Identifying the Factors Impacting the Performance of Two-Axis Sun-Tracking Photovoltaic Systems on Mobile Platforms

Ryan Coble-Neal

School of Civil &. Mechanical Engineering Project Thesis
Curtin University

13/06/2024

13/06/2024

The Head
School of Civil & Mechanical Engineering,
Curtin University,
Kent Street,
Bentley,
WA 6102

Dear Sir,

I submit this thesis entitled “Identifying the Factors Impacting the Performance of Two-Axis Sun-Tracking Photovoltaic Systems on Mobile Platforms”, based on MXEN4000 Mechatronic Engineering Research Project 1 and MXEN4004 Mechatronic Engineering Research Project 2, undertaken by me as part-requirement for the degree of B.Eng (Hons) in Mechatronic Engineering.

Yours faithfully,

Ryan Coble-Neal
19182641

ACKNOWLEDGEMENTS

Thanks to Dr. Chris Ford for supervising this thesis, and thanks to Cameron Duncan for allowing me to use his 3D printer to print parts for the experiment.

ABSTRACT

There are many applications for photovoltaics on mobile platforms from personal vehicles to logistics and public transportation with some studies finding significant merit in their application. The ability to generate power anywhere without emitting greenhouse gases is attractive for decarbonising transport particularly as the cost of fossil fuels increases due to the removal of subsidies and the imposition of emissions taxes. At the same time there are tax incentives on offer to switch to more efficient combustion engines and even bigger tax incentives for hybridisation and electrification. This is particularly notable in cold chain mobile logistics where refrigerated goods are transported by vehicles operating transport refrigeration units that are ordinarily powered by the diesel engine of the vehicle itself. The performance of photovoltaic panels can be greatly improved with Sun-tracking as the angle between the direction of sunlight and the normal of the panel is the biggest factor that determines how much solar energy is available to convert into electricity. In this thesis the major factors that impact the performance of photovoltaic panels are identified, and the key considerations on locomotive performance of mobile platforms are outlined. In the process of identifying these factors a significant gap in the literature regarding actuation systems for Sun-tracking on mobile platforms is identified.

Pages 2 – 19 of this thesis contain material that was previously submitted as part of the Progress Report assessment for the MXEN4000 Mechatronic Engineering Research Project 1 unit.

TABLE OF CONTENTS

1.0 INTRODUCTION

The objectives of this project are as follows:

1. Create a simple solar model to evaluate the available solar energy at the latitude where the experimentation will take place.
2. Calculate the expected solar energy for different configurations of photovoltaic (PV) panels using the data from the model.
3. Validate the model with experimental data.
4. Identify the most important factors that influence the performance of photovoltaic panels on mobile platforms.

Through modelling solar equations and making use of simplifying assumptions regarding weather and environmental conditions a maximum energetic gain of 35.05% is found for a two-axis Sun-tracking surface compared to a horizontal surface. The solar model predicts that the greatest influence on power generation is the angle of incidence between the normal of a PV panel and the direct beam component of irradiance. An experiment designed to simulate the effect of a mobile platform such as a car being oriented such that it is facing Southward (away from the Sun at the testing site) and on an incline (also Southward) is carried out. Three configurations of PV panels are tested alongside a control experiment demonstrating a maximum gain in average short circuit current of 85.64% by use of two-axis Sun-tracking.

Through the literature review a significant gap in the literature regarding actuation systems for two-axis Sun-tracking suitable for mobile platforms is identified while the key governing equations impacting the locomotive performance are derived. There is a need for further research into actuation systems capable of stowing flat during transit to minimise drag while still being able to achieve full range of motion of two-axis Sun-tracking.

2.0 LITERATURE REVIEW

2.1 Applications for Photovoltaics in Mobile Platforms

2.1.1 Personal Vehicles

The idea of vehicle integrated photovoltaics has inspired many concept designs and commercial products from the Lightyear 2 (Lightyear n.d.), the Stella Terra and Vita (Smolenaars 2021), and the various entrants to the Bridgestone World Solar Challenge (World Solar Challenge n.d.). While a plethora of examples of the application of vehicle integrated photovoltaics exist in the automotive industry, there are few retrospectively installable PV systems available to consumers. This leaves most consumers who are unable to access products like those mentioned earlier having to attempt to design and install their own PV systems to meet their requirements as seen in Figures 1 and 2 below.

Figure 1. Ryan Coble-Neal, *Fixed tilt photovoltaic panels on 4WD at night.* 2023, Digital Image. CC BY-SA 2.0

Figure 2. Ryan Coble-Neal, *Fixed tilt photovoltaic panels on 4WD.* 2023, Digital Image. CC BY-SA 2.0

The most common types of vehicles using roof-mounted PV panels include cargo vans, utility vehicles, special utility vehicles, off-road vehicles like the 4WDs in the figures above, and in less frequent occurrence, sedans, and buses. Most of these vehicles use PV panels for powering recreational activities, however some vehicles (mainly cargo vans) are dependent on PV power systems to power appliances used in domestic living. This is commonly referred to as ‘van-life,’ meaning people who live and work in cargo vans, although it is also becoming a popular and cost-effective way for tourists to travel (Australian Broadcasting Corporation 2021).

The purpose of these PV systems tends to be to charge a single lead acid accumulator battery, or a lithium-ion based battery system. This power is then used to run

appliances such as small DC refrigerators, coffee machines and other low wattage appliances, but can also be used to power recovery winches. Some installations involve higher powered PV systems, DC-DC converters, maximum power point trackers (MPPTs) and battery management systems with larger batteries that then provide a series of DC buses for various common voltages. It is also common to find an inverter in a system like this which provides standard grid specification AC power via a dedicated AC bus for appliances that cannot be easily converted to run on DC power. Such AC appliances include electric kettles, inductive cook tops, microwaves, hot water systems, TVs, radio systems, internet connection devices such as Starlink and routers, and in some cases electric ovens. Beyond just recreational and lifestyle applications of roof-mounted photovoltaics on standard commercially available vehicles, there are other types of mobile platforms that require electricity.

2.1.2 Transport Refrigeration Units

Logistics vehicles such as box trucks often operate energy intensive cooling systems for transporting fresh produce and refrigerated goods. The cooling system is called a transport refrigeration unit (TRU) and is employed in a variety of mobile platforms including rail cars, semi-trailers, and shipping containers as well as box trucks. TRUs are powered in a variety of ways including directly from the internal combustion (IC) diesel engine, an integrated diesel genset, a plug-in hybrid electric/diesel combination and a fully electric TRU known colloquially as an eTRU (United States Environmental Protection Agency 2022). In the context of rail cars and shipping containers it is common to find the power source to be a dedicated rail car with a series of diesel gensets known as a ‘powerpack,’ and on-board ship electrical power respectively.

It is predicted that given the expected population growth rate up to the year 2050, the requirement for cooling will grow by a factor of 10 (Deutsche Gesellschaft für Internationale Zusammenarbeit (GIZ) GmbH 2022) (She, et al. 2018). This accounts for all cooling, not just that required by TRUs for the cold chain (the refrigerated supply chain), however a growing population that is increasingly inhabiting urban centres requires a greater food supply to be transported over more distance.

Transporting perishable items and products that require freezing, such as medication, through greater distances from more distant production and distribution centres to, and through, bigger and bigger urban centres with more stops exponentially increases the total TRU energy requirement. Particularly when it comes to intra-urban centre travel with multiple stops, where at each stop a significant portion of the refrigeration of the cargo area is lost, the energy requirement and accompanying GHG emissions are significantly higher.

Figure 3 below illustrates a simplified model of a cargo van that incorporates a direct IC engine powered TRU and shows the various sources of heat flow during standard operation.

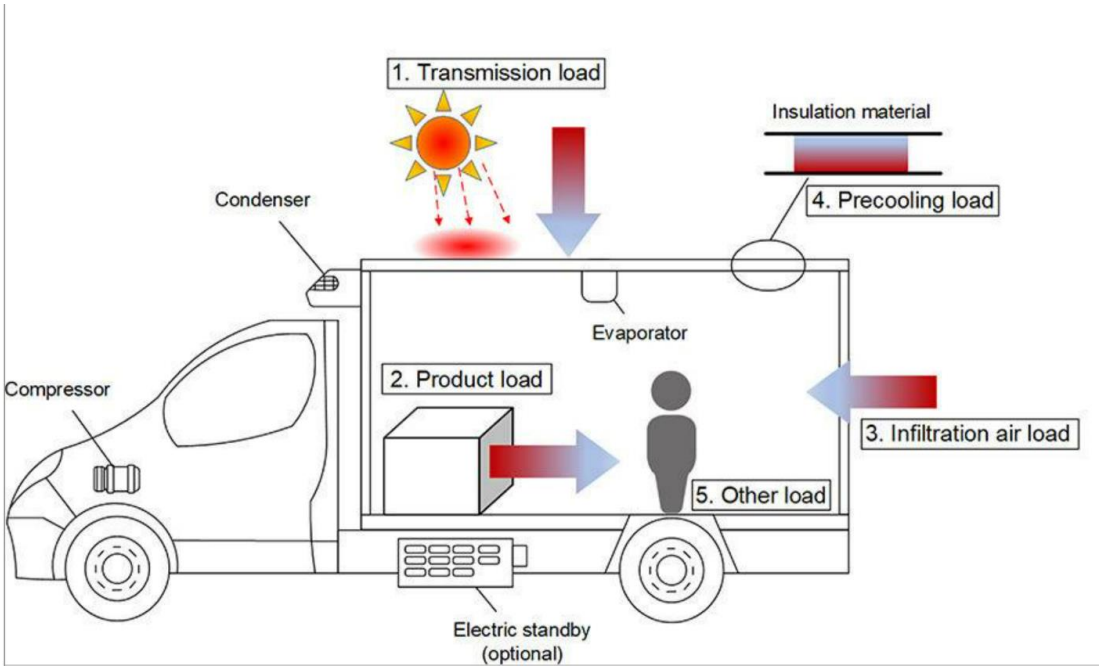

Figure 3. Main sources of heat in refrigerated van.

Source: Figure reproduced from (Yang , et al. 2021).

Following on from the simplified model of heat transfer in Figure 3 are the modelled CO_2 and NO_X emissions related to the main contributing factors that impact the energy requirement from the IC diesel engine for refrigeration, shown in Figure 4 below. Note that the PHEM model (version 13.0.3.21), which is an instantaneous vehicle emission model, was used in the referenced study (Yang , et al. 2021).

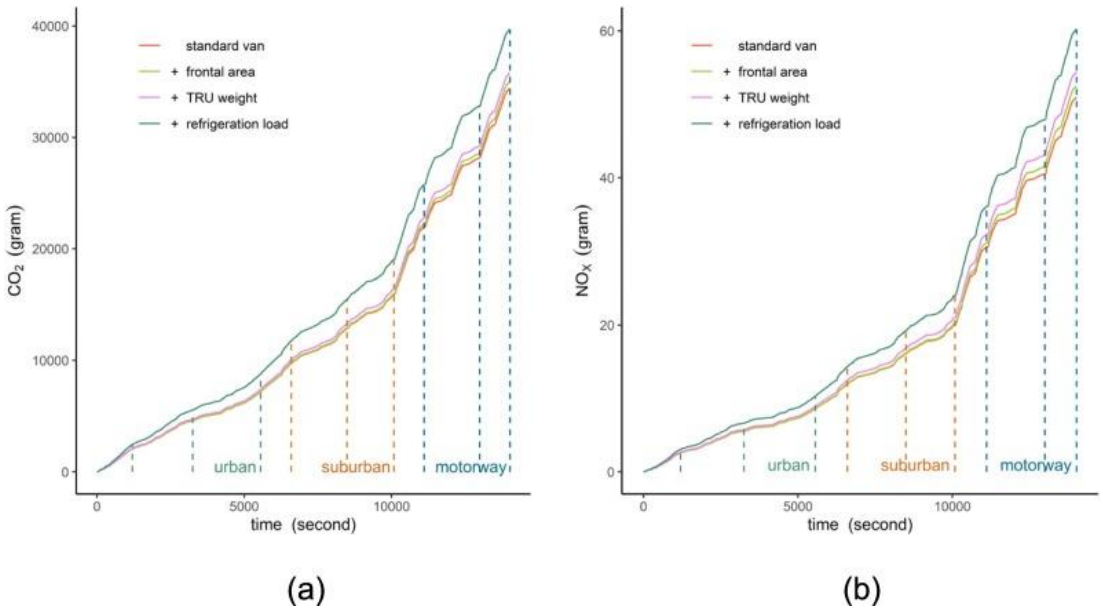

Figure 4. Cumulative plot of (a) CO_2 emissions (left) and (b) NO_X emissions (right) at an ambient temperature of 20 °C (different parts of TRU load).

Source: Figure reproduced from (Yang , et al. 2021).

From the graphs in Figure 4 it can be seen that the impact on GHG emissions due to the additional energy requirement for the refrigeration load was the greatest component even when compared with the additional weight and aerodynamic drag of the TRU itself. Supporting this, Table 1 shown below relates the impact of ambient temperature to the percentage share of additional emissions of these same factors.

Table 1: Impact on the CO_2 and NO_X emissions by various ambient temperature

Pollutant	Ambient temperature, °C	Emission rates, g/km	Share of different parts in additional emissions		
			Frontal area	TRU weight	Refrigeration load
CO_2	40	297	8%	10%	82%
	20	282	11%	14%	74%
	0	265	21%	26%	53%
NO_X	40	0.45	12%	16%	72%
	20	0.43	16%	21%	62%
	0	0.40	27%	35%	38%

Source: Table reproduced from Yang, et al. 2021.

The refrigeration load (which increases with increasing ambient temperature) is by far the greatest contributor to additional emissions of cargo vans when the TRU is powered directly by the IC diesel engine of the vehicle. This additional energy requirement is exacerbated by the frequency and duration of cargo doors being opened especially when routes have more and more stops. Concerningly, it has been found that auxiliary engine powered TRUs, i.e., TRUs that have their own dedicated diesel genset which are commonly used in larger vehicles such as rigid trucks and semi-trailers, in the UK, emit 16 times as much NO_X and 40 times as much particulate matter per kWh of energy than the locomotive engine of the truck itself (cenex 2021).

While the environmental impact of diesel powered TRUs is clear, the economic impact is also significant, especially in the UK. In 2020 the UK government removed the entitlement of certain vehicles using diesel, which included mobile generators such as TRUs, to the red diesel subsidy, which was responsible for subsidising the tax on diesel, from 57.95 pence ($1.12 AUD)/L to 11.14 pence ($0.21 AUD)/L (cenex 2021). As a result, the fuel cost of operating auxiliary engine powered TRUs that use diesel for energy generation are now subject to an additional 80.78% tax cost.

Beyond taxes, it is also reasonable to expect fuel prices to continue to rise over the next few decades due to the scarcity of easily accessible fuel reserves leading to more expensive extraction to match an increasing worldwide demand for energy. In an oppositely incentivised approach, the Environmental Protection Agency (EPA) in the United States passed the Diesel Emissions Reduction Act (DERA) which includes a funding scheme that includes emissions reductions of TRUs. Part of the scheme is that the EPA will fund up to 25% of the replacement cost of TRUs to be replaced with more modern diesel or hybrid TRUs with engines meeting the EPAs emissions standards (United States Environmental Protection Agency 2022). Further to this, the EPA offers to fund up to 45% of the cost of an eligible zero-tailpipe emission TRU, among a variety of other funding schemes for stationary refrigeration systems, plug-in/shore power and inductive recharging bay expenses as well (United States Environmental Protection Agency 2022).

Given the various environmental and economic incentives to move toward decarbonising TRUs, some groups have begun working out how this could be achieved at scale. The use of hydrogen as a fuel source in a proton-exchange membrane fuel cell (PEMFC) has been modelled and a feasibility study has been conducted in a European context. The result of the feasibility study was that over a 20-year project, inclusive of the cost of hydrogen production and refuelling infrastructure, at least €400,000 of savings could be expected when compared with continuing to operate diesel powered TRUs for the same use case and time period (Garde, et al. 2012). Further to this, the study also anticipates being able to prevent up to 21 tonnes of CO_2 emissions per truck per year. While these numbers are very encouraging, the authors do point out that the lack of existing infrastructure remains a barrier to the adoption of fuel cell technology for this purpose.

In another approach also investigating a European context, roof mounted PV panels with an accompanying Li-ion battery pack replacing an auxiliary diesel engine on a standard semi-trailer were modelled. The overall system energy generation and cost performance was evaluated for a specified route, and it was found that up to 89% of GHG emissions could be prevented equating to 9572 $kgCO_2Eq/yr$ per vehicle (Meneghetti, Magro and Romagnoli 2021). The accompanying payback period for the system was expected to be six years, although the authors anticipate a much shorter payback period as components such as PV panels and Li-ion batteries continue to fall in price in the next decade.

2.1.3 Mass Public Transportation

Another area of interest for electrification of mobile platforms is in mass urban transit. While trains and trams tend to be powered by overhead grid-fed lines, buses remain an unsolved problem in this regard. A study carried out in a Middle Eastern context proposed the use of PV panels to provide energy for tractive effort of buses but further proposed the configuration of the PV panels to improve aerodynamic performance of buses. In the first proposed configuration of roof-mounted PV panels, the panels are oriented on a fixed angle of attack on the roof of the bus and the unit cost of energy and vehicle specific power were found to be 0.922 $/kWh and 12.71

kW/t respectively (Ifaei, et al. 2020). In the other configuration, making use of the frontmost PV panels to improve aerodynamic efficiency, the values were respectively 0.864 $/kWh and 17.53 kW/t. Like the aforementioned study, this study proposed a valid feasibility study and modelled a number of pertinent factors that impact PV performance such as dust, total irradiance, and de-rating factor. The impact of aerodynamic drag and mass were also accounted for and compared against meaningful base cases.

2.2 Main Factors Impacting Performance of PV Panels

Broadly, the performance of PV panels (also known as modules) at any instant in time is dictated by two main factors: The amount of solar irradiance incident upon the photovoltaic material, and the overall module conversion efficiency. Note that there is a subtle, but key distinction between the amount of solar irradiance incident upon a PV panel and the amount of solar irradiance incident upon the photovoltaic material of a PV panel.

2.2.1 Solar Irradiance

Irradiance (W/m^2) is a measure of the intensity of power in radiation per unit area. Direct normal irradiance (DNI) is the direct beam irradiance from the Sun as measured at the surface of Earth, while global horizontal irradiance (GHI) is a measure of the total irradiance incident upon a horizontal surface. The GHI is comprised of the angular component of DNI as well as the diffuse horizontal irradiance (DHI), which comes from diffuse light scattered by the atmosphere and clouds. When taking the average of irradiance over time, the insolation (or irradiation) (Wh/m^2), which is the total energy of incident radiation upon a unit area, is found. The global averages of GHI and DNI (insolation) are shown in Figures 5 and 6 below.

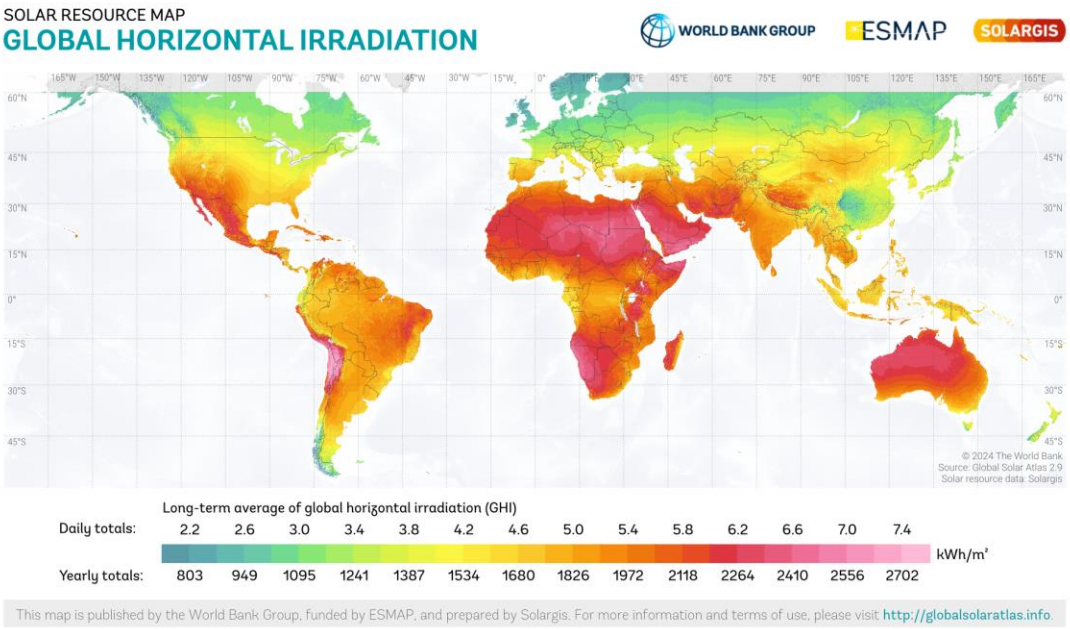

Figure 5. Global horizontal irradiation.

Source: Figure reproduced from (Solargis 2021).

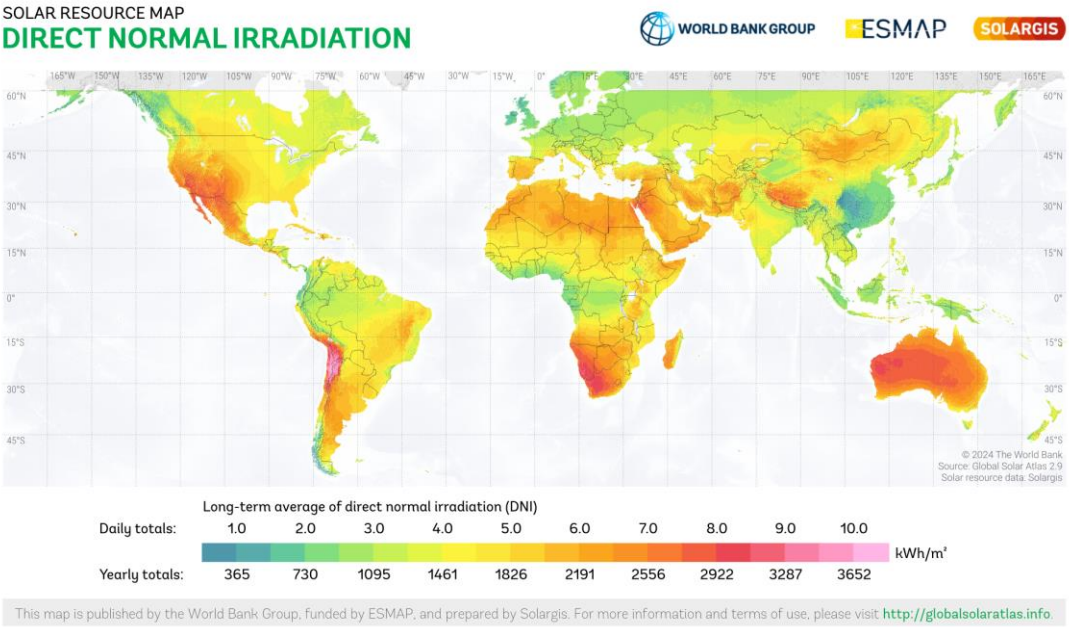

Figure 6. Direct normal irradiation.

Source: Figure reproduced from (Solargis 2021).

In order to calculate solar irradiance values at a particular site on Earth, the relative position of the Sun and angles from the reference point on Earth must first be calculated. Due to the change in the angle of solar declination over the course of the year, in Winter the intensity of solar irradiance is less, conversely in Summer the intensity is greater. The same case is true for both the Southern and the Northern hemispheres, and this phenomenon is due to the fact that the Earth is tilted by ~23.45° with respect to the plane upon which it orbits the Sun. This is visualised in Figure 7 below, along with some key dates including the solstices and equinoxes.

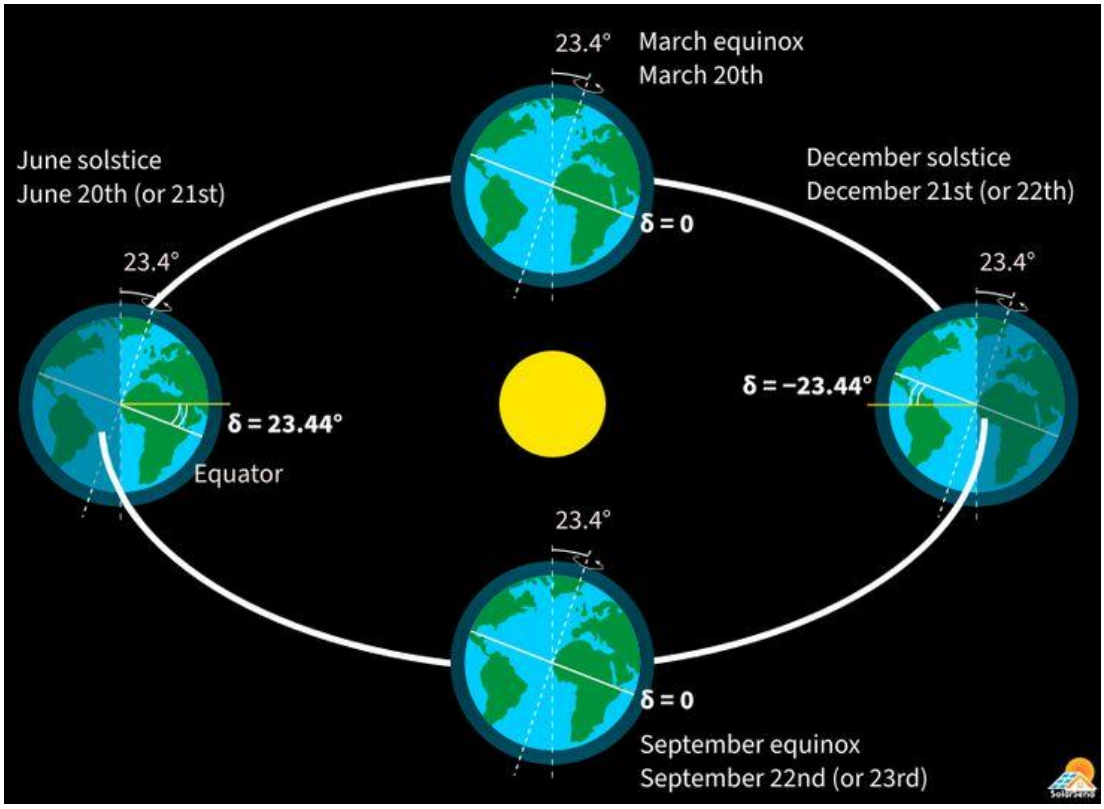

Figure 7. Solar declination angle.

Source: Figure reproduced from (Solar Sena 2021).

The June and December solstices represent the dates at which solar irradiance is perpendicular to the tropics of Cancer and Capricorn respectively i.e., the Sun appears directly overhead at the respective tropic. The equinoxes represent the dates at which all points on Earth experience 12 hours of daylight and 12 hours of night, during which time the Sun will appear directly overhead at the equator at solar noon. The equation for calculating the solar declination angle for any given day of the year is given in Equation 1 below (Masters 2013).

$$\delta = 23.45sin\left[\frac{360}{365}(n-81)\right] \quad (1)$$

'δ' is the solar declination angle in degrees, and 'n' is the day number of the year e.g., January 1st would be n = 1.

The next solar equation needed is the hour angle, which is the number of degrees the Earth must rotate about its axis (Eastward) before the Sun will be directly overhead at a given local meridian (line of longitude) (Masters 2013). Hence, the difference between the Sun's meridian and the local meridian is the hour angle, which is visualised in Figure 8 below.

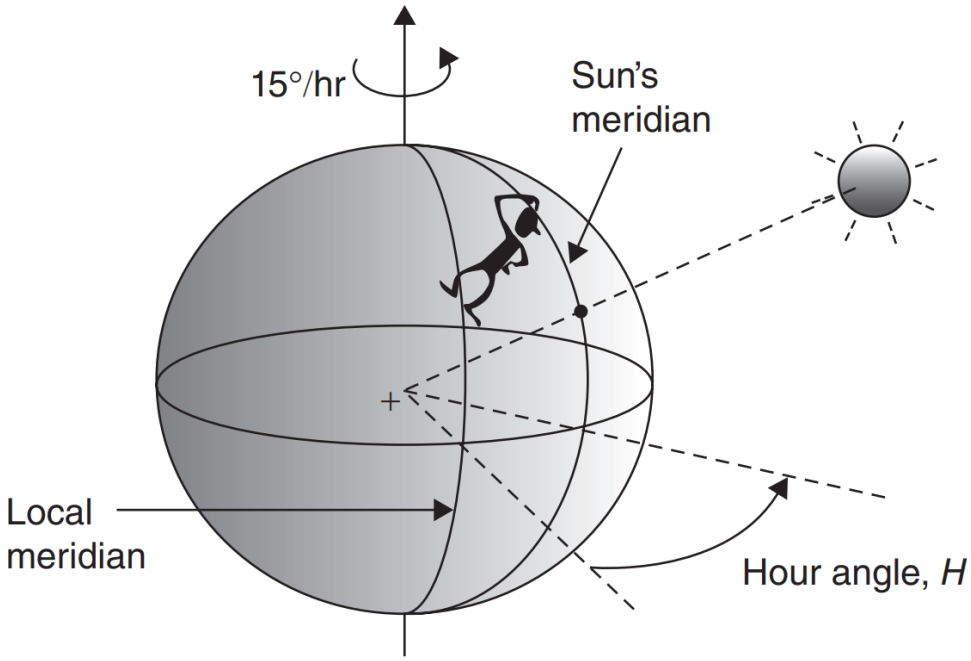

Figure 8. The hour angle is the number of degrees the Earth must turn before the Sun is directly over the local meridian. It is the difference between the Sun's meridian and the local meridian.

Source: Figure reproduced from (Masters 2013).

The convention used here is that hours before solar noon (which is when the Sun is directly overhead) are taken to be positive and vice versa e.g., 10am local solar time (ST) corresponds to +2 hours, while 2pm corresponds to -2 hours. Finally, since the Earth rotates 360° per day (4 minutes per degree), and there are 24 hours in a day, it follows that one hour corresponds to 15° in regard to the hour angle. Equation 2 below shows the hour angle calculation (Masters 2013).

$$H = \left(\frac{15°}{hour}\right) \times Hours\ before\ solar\ noon$$

$$\rightarrow H = \left(\frac{15°}{hour}\right) \times (12 - Solar\ Time) \quad (2)$$

The Earth is nominally divided into 24 time zones (UTC) each covering 15° of longitude with the clock time (CT) set to be the same across the entire time zone. When the position of the Sun is required at any clock time and location on Earth, a conversion between the clock time at the local time zone (or local time meridian) and solar time is required shown in Equation 3 below (Masters 2013).

$$ST = CT + \frac{4\,min}{degree}(Local\ Time\ Meridian - Local\ Longitude)° + E(\text{min}) \quad (3)$$

'ST' is solar time (hours), 'CT' is clock time (hours) (add 1 hour if daylight savings time is in effect), 'local time meridian' is the longitude of the time zone, 'local longitude' is the longitude of an observer within that time zone, and 'E' is the equation of time (minutes), which is shown later. An important note here is that most solar energy textbooks treat longitude as positive when West of the Prime Meridian in the range 0° < longitude < 360°. However, the UTC time zones treat longitude as positive when East of the Prime Meridian from 0° < longitude < 180° E, and negative when West from -180° W < longitude < 0°. Thus, Equation 3 should be used for longitudes West of the Prime Meridian (UTC < 0) and should be rearranged as shown in Equation 3.1 below for longitudes East of the Prime Meridian (UTC > 0).

$$ST = CT + \frac{4\,min}{degree}(Local\ Longitude - Local\ Time\ Meridian)° + E(\text{min}) \quad (3.1)$$

For a concrete example, take two locations both showing clock time (CT) = 12pm on January 1st: Boston (longitude = 71°W, UTC = -5 i.e. local time meridian = -5 × 15° = 75°W), and Perth (longitude = 115°E, UTC = +8 i.e. local time meridian = 8 × 15° = 120°E). The equation of time 'E' is the same for both locations and is -3.6 mins. The solar time (ST) for Boston (using Equation 3) is 12:12pm, and in Perth (using Equation 3.1) it's 11:36am. Therefore, the hour angle 'H' in Boston (using Equation 2) is -3°, and in Perth it's +6°.

The Equation of Time (E) (in minutes) which accounts for the slightly elliptical orbit of the Earth around the Sun which causes the length of a solar day (solar noon to solar noon) to vary throughout the year is found with Equations 4 and 4.1 below (Masters 2013).

$$E = 9.87\sin(2B) - 7.53\cos(B) - 1.5\sin(B) \quad (minutes) \tag{4}$$

$$B = \frac{360}{364}(n - 81) \quad (degrees) \tag{4.1}$$

'B' is an empirical parameter (degrees). Using the equations for solar declination and hour angle from Equations 1 and 2 respectively, the elevation angle (sometimes referred to as altitude angle), which is the vertical angle between the local horizon of a site and the Sun can be calculated in Equation 5 below (Masters 2013).

$$sin(\beta) = cos(L)cos(\delta)cos(H) + sin(L)sin(\delta) \tag{5}$$

'β' is the elevation angle in degrees and is obtained by taking the inverse sine of the result of the equation while 'L' is the latitude angle, with latitudes North of the equator positive and South of the equator negative. A negative elevation angle implies that the Sun is below the local horizon. Extending the earlier example using Boston (latitude = 42° N) and Perth (latitude = -32° S), the elevation angle at 12pm clock time would be ~25° and ~80° respectively.

Another important note is that the elevation angle is within the range of $0° < \beta < 90°$. In latitudes between the tropics of Cancer (23.45° N) and Capricorn (-23.45° S) the Sun will appear in the Southern or Northern sky depending on the day of the year. A useful trick to work out whether the Sun will be in the Northern or Southern sky for a given latitude between the tropics on a given day of the year is to set the angle of solar declination equal to the latitude angle from Equation 1 as shown below.

$$\delta = L = 23.45sin\left[\frac{360}{365}(n - 81)\right] \tag{1.1}$$

This can be rearranged in terms of the day number 'n' which yields two values due to the arcsine.

$$n_1, n_2 = 81 + \frac{365 \sin^{-1}\left(\frac{L}{23.45}\right)}{360} \tag{1.2}$$

On day numbers n_1 and n_2 (where $n_2 > n_1$) the Sun will be directly overhead, and from day numbers n_1 to n_2 when $\delta > L$ the Sun will appear in the Northern sky at solar noon. For all other days of the year outside of the range from n_1 to n_2 the Sun will appear in the Southern sky at solar noon. This is useful for sanity checking the calculated azimuth and elevation angles for latitudes between the tropics.

The azimuth angle is the horizontal angle between the Sun and an observer, which is measured from North (but can be measured from South), and can be calculated using the sign convention that North is taken to be 0° with the azimuth angle being positive in the Eastward direction up to 180° and negative in the Westward direction up to -180°. The first part of the calculation to determine the azimuth angle is given in Equation 6 below (Masters 2013).

$$sin(\varphi_s) = \frac{cos(\delta)sin(H)}{cos(\beta)} \tag{6}$$

'φ_s' is the azimuth angle of the Sun and the value in degrees is obtained by taking the inverse sine of the result of the equation. However, a check is required to be used to determine the correct value for the azimuth angle as the arcsine yields two possible answers. This check is carried out in the form of an inequality test between the ratio of tangents of the solar declination and latitude angles against the cosine of the hour angle as shown below in Equation 6.1 (Masters 2013).

$$If\ cos(H) \geq \frac{tan(\delta)}{tan(L)}, \qquad then\ |\varphi_s| \leq 90°, \qquad else\ |\varphi_s| > 90° \tag{6.1}$$

These equations form the basis for calculating the angle of incidence between the direct beam component of solar irradiance and the normal of a PV panel. However, for the case of a PV panel that is horizontal and flat with respect to the ground, the

angle of incidence is just the sine of the elevation angle as shown in Equation 7 below (Masters 2013).

$$\theta = sin(\beta) \tag{7}$$

'θ' is the angle of incidence in degrees. For the case of tilted PV panels that have their own azimuthal orientation and tilt angle, the angle of incidence is calculated using Equation 8 below (Masters 2013).

$$cos(\theta) = cos(\beta)cos(\varphi_s - \varphi_c)sin(\Sigma) + sin(\beta)cos(\Sigma) \tag{8}$$

'φ_c' is the azimuth angle of the PV panel in degrees and 'Σ' is the tilt angle of the PV panel in degrees measured upward from the horizontal plane. With the requisite solar angle equations, the components of solar irradiance including the incident direct beam, diffuse, and reflected components can be found. The total beam of irradiance is characterised by an exponential attenuation of apparent extra-terrestrial flux i.e., the solar irradiance measured at the top of the Earth's atmosphere, with respect to the distance between the Sun and Earth. Other attenuating factors include optical depth and air-mass index, which are measures of air quality and the ratio of the distance/amount of the atmosphere through which the beam must pass respectively. The calculation of apparent extra-terrestrial flux is provided in Equation 9 below (Masters 2013).

$$A = 1160 + 75sin\left[\frac{360}{365}(n - 275)\right] \tag{9}$$

'A' is apparent extra-terrestrial flux in W/m^2. As seen by the inclusion of the day number of the year 'n', it can be seen that the apparent extra-terrestrial flux changes throughout the year. This is due to the slightly elliptical orbit of the Earth around the Sun causing there to be periods of the year during which the Earth is closer to the Sun and hence the intensity of solar irradiance is greater, and vice versa.

The equation of the attenuating factor of optical depth is provided in Equation 10 below (Masters 2013).

$$k = 0.174 + 0.035sin\left[\frac{360}{365}(n - 100)\right] \quad (10)$$

'k' is optical depth and is unitless. The air-mass index, which is a measure of how much atmosphere a beam of solar irradiance must travel through is calculated by Equation 11 below (Masters 2013).

$$m = \frac{1}{\sin(\beta)} \quad (11)$$

'm' is the air-mass index and is unitless, however it is useful to note that it is inversely related to the sine of the elevation angle meaning that for low values of the elevation angle i.e., in the mornings and evenings, the air-mass index is greatest. Given these equations, the direct beam component of terrestrial solar irradiance can be calculated using Equation 12 below (Masters 2013).

$$I_B = Ae^{-k \cdot m} \quad (12)$$

'I_B' is the direct beam of solar irradiance in W/m^2 measured at the ground on Earth. It can be seen that the direct beam is the result of attenuation of the extra-terrestrial flux available from the Sun as a function of the extra-terrestrial distance, quality, and amount of atmosphere. The beam component of irradiance incident upon a PV panel is proportional to the direct beam of solar irradiance and the cosine of the angle of incidence between the normal of a PV panel and the direct beam of solar irradiance. In the case of a horizontal PV panel, the calculation of the incident beam component of irradiance is calculated using Equation 13 below (Masters 2013).

$$I_{BH} = I_B \sin(\beta) \quad (13)$$

'I_{BH}' is the incident beam component of irradiance upon a horizontal PV panel in W/m^2. The beam component of irradiance incident upon a tilted collector is given in Equation 14 below (Masters 2013).

$$I_{BC} = I_B \cos(\theta) \tag{14}$$

'I_{BC}' is the beam component of irradiance incident upon a tilted PV panel in W/m^2. The cosine of the angle of incidence is sometimes referred to as the cosine effect. A useful intuition is simply that as the angle of incidence increases up to 90 degrees, the incident beam component of irradiance decreases to 0. The incident beam component of solar irradiance is usually, by an order of magnitude, the most power dense component of solar irradiance, however the diffuse component can comprise a significant portion of the total power of solar irradiance. There is an argument to be made for tracking systems to optimise both the diffuse and direct beam components, however this has been found to only yield an additional 2% energy generation (Gordon, Kreider and Reeves 1991). In the case of horizontal PV panels however, the diffuse component is considerable as the flat orientation of the panel maximises the field of view for collection of diffuse irradiance. This is because it is typically assumed that diffuse irradiance is isotropic in nature. The calculation of the diffuse component of solar irradiance as a proportion of the beam irradiance depends on the sky diffuse factor which is estimated by Equation 15 below (Masters 2013).

$$C = 0.095 + 0.04sin\left[\frac{360}{365}(n - 100)\right] \tag{15}$$

'C' is the sky diffuse factor and is unitless. The sky diffuse factor provides a useful approximation of diffusion as a function of the day of the year. Using this sky diffuse factor, the diffuse component of irradiance on a horizontal PV panel can be calculated using Equation 16 below (Masters 2013).

$$I_{DH} = CI_B \tag{16}$$

'I_{DH}' is the diffuse component of irradiance on a horizontal collector in W/m^2. In the case of a tilted mono-facial PV panel the diffuse component of irradiance is proportional to the tilt angle as characterised by Equation 17 below (Masters 2013).

$$I_{DC} = I_{DH}\left(\frac{1+\cos(\Sigma)}{2}\right) = CI_B\left(\frac{1+\cos(\Sigma)}{2}\right) \tag{17}$$

'I_{DC}' is the diffuse component of irradiance upon a tilted PV panel in W/m^2. The diffuse component of irradiance upon a tilted PV panel is represented using the expansion of the diffuse component of irradiance upon a horizontal PV panel to parameterise it in terms of the beam of irradiance. This is done for the sake of generating one computation that applies a series of factors to the beam of irradiance which will be shown later. The final component of irradiance is the reflected irradiance which is calculated using Equation 18 below (Masters 2013).

$$I_{RC} = \rho(I_{BH} + I_{DH})\left(\frac{1-\cos(\Sigma)}{2}\right) = \rho I_B[\sin(\beta) + C]\left(\frac{1-\cos(\Sigma)}{2}\right) \tag{18}$$

'I_{RC}' is the component of reflected irradiance incident upon a tilted PV panel in W/m^2, 'ρ' is the reflective index/reflectance of the surrounding surfaces and is unitless. The reflective index tends to lie somewhere between 0.1 and 0.8 where something like grass tends to have a value of 0.2 while fresh snow has a value of 0.8. While the reflected irradiance tends to be the weakest component of irradiance it is still worth including, although it should be noted that for a horizontal PV panel the reflected irradiance is zero because the tilt angle is zero. Finally, the total irradiance on a tilted PV panel is calculated using Equation 19 below (Masters 2013).

$$I_C = I_{BC} + I_{DC} + I_{RC} \tag{19}$$

$$\rightarrow I_C = Ae^{-k\cdot m}\left[cos(\beta)cos(\varphi_s - \varphi_c)sin(\Sigma) + sin(\beta)cos(\Sigma) + C\left(\frac{1+\cos(\Sigma)}{2}\right) + \rho[\sin(\beta) + C]\left(\frac{1-\cos(\Sigma)}{2}\right)\right]$$

'I_C' is the total irradiance incident upon a PV panel that can be horizontal or otherwise oriented, in W/m^2.

From Equations 1 – 19 the main finding is that the total incident irradiance upon a PV panel is dependent upon the distance between the Sun and the Earth, the angle of incidence between the normal of the PV panel and the components of solar irradiance, the time of day and day of year, amount of atmosphere and cloud cover. The relationship between irradiance, current and overall power generated by a PV panel is directly proportional as seen below in Figure 9.

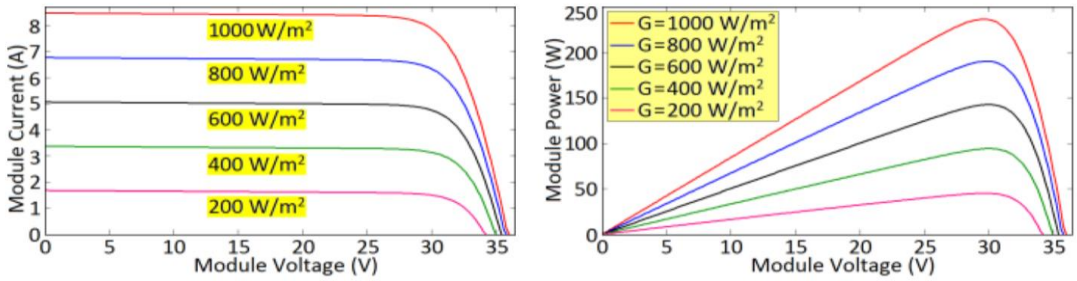

Figure 9. Impacts of variations in irradiance on the current and output power of a PV module.

Source: Figure reproduced from (Vidyanandan 2017).

2.2.2 PV Panel Reflectance

Most modern PV panels make use of deeply textured glass and antireflective coatings (ARCs) to reduce the amount of reflection at the air-glass interface, and within the panel as silicon is reflective. It has been found in multiple numerical, analytical and empirical studies that for angles of incidence greater than 55°, the reflectance of most commercially available PV panels increases exponentially (ForgeSolar n.d.), (Janakeeraman 2013), (Yellowhair and Ho 2015), (Dynge and Stoveland 2013), (King, Boyson and Kratochvill 2004), (King, Boyson and Kratochvil 2002). This results in the light transmission factor, which is the ratio of absorbed flux in PV cells divided by the incident flux on the PV panel surface, dropping at approximately the same rate. Both of these relationships are depicted in Figures 10 and 11 below.

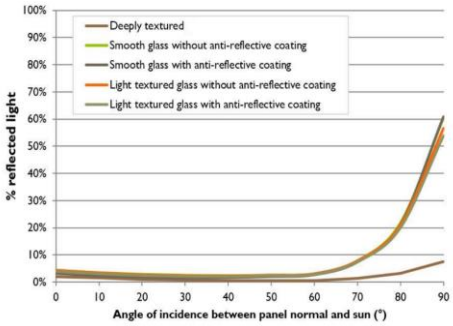

Figure 10. Reflectance profiles of typical PV module materials.

Source: Figure reproduced from (ForgeSolar n.d.).

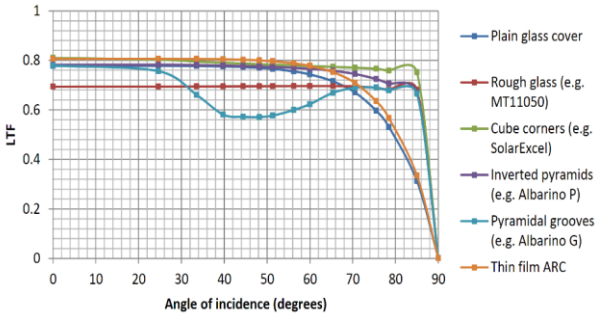

Figure 11. Light transmission factor as a function of angle of incidence for the PV model with the different glass covers

Source: Figure reproduced from (Dynge and Stoveland 2013).

The loss of irradiance due to reflection as a function of angle of incidence between the normal of a PV panel and each component of solar irradiance is characterised in Equation 20 below (Martin and Ruiz 2005).

$$AL(\alpha) = 1 - \frac{1 - \exp\left[-(\cos\theta)/\alpha_r\right]}{1 - \exp\left(-1/\alpha_r\right)} \tag{20}$$

Where 'AL' is angular loss factor, and 'α_r' is the angular loss coefficient, which is an empirical dimensionless parameter dependent on the technology of the PV module. Typical values for α_r range from 0.16 to 0.17 for commercial clean polycrystalline and amorphous silicon modules respectively with these values being inclusive of anti-reflective coatings. This model of angular loss has been applied to data from 79 different sites during meteorologically representative years at latitudes from -80 º to +80.6º with different tilt angles in steps of 10º from 0º to 90º and a fixed azimuth angle, i.e., 0º and 180º in the respective hemispheres. After corrections for local variations due to weather effects, the annual angular loss data as a function of the difference of the absolute value of latitude angle and tilt angle was compiled as seen in Figure 12 below.

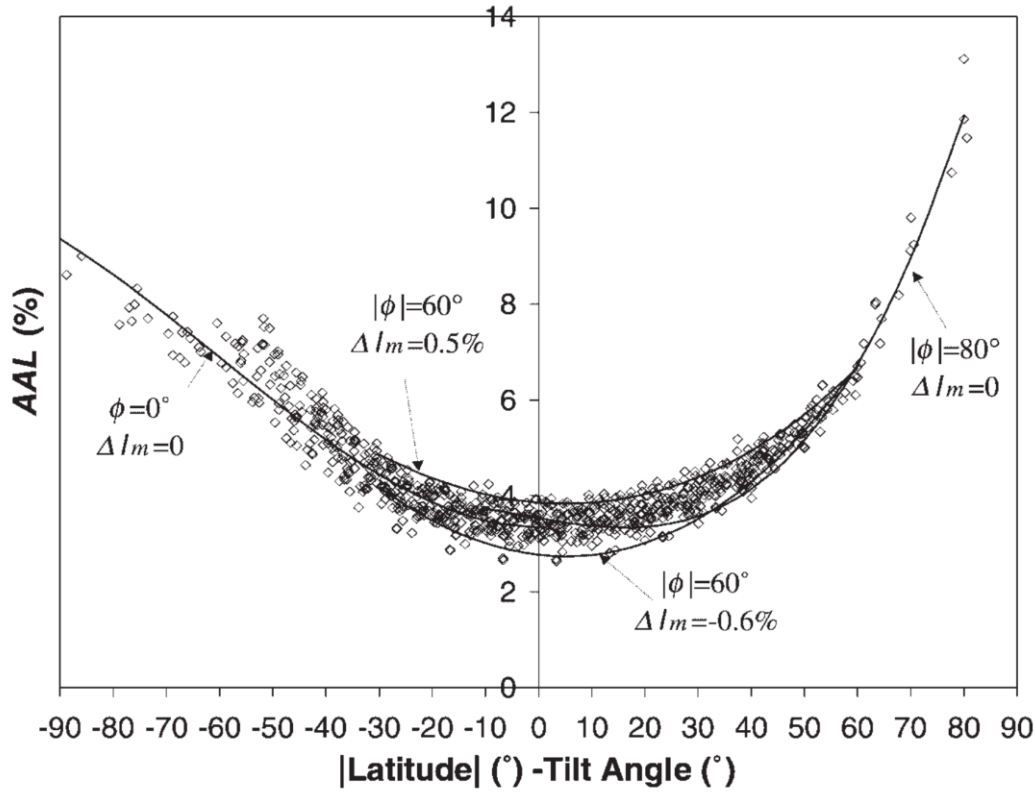

Figure 12. Calculated AAL of a PV clean module at 79 different sites at tilt angles of 0–90, in steps of 10 (equator oriented), plotted against the difference |latitude| – tilt angle. The curves correspond to the predicted AAL by the mixed model at four locations, characterised by ∅ and Δlm.

Source: Figure reproduced from (Martin and Ruiz 2005).

The horizontal axis shows the difference between the absolute value of latitude angle and the tilt angle (from 0 to 90º), which implies that 0º on the horizontal axis corresponds to a tilt angle of the PV module equal to the latitude angle. Conversely, +90º implies that the tilt angle is set to 0º and that the latitude is extremely far from the equator. At -90º the tilt angle is set to 90º at the equator. For a latitude such as that of Perth (-32º S), a horizontal PV panel (tilt angle = 0º) would suffer an annual angular loss of approximately 4%.

2.2.3 PV Panel Soiling

The effect of soiling of PV panels by dust or other particles contributes to reflectance and can be approximated by the same parameters in Equation 20 from earlier. The typical values of α_r can increase to approximately 0.2 when the module is moderately soiled with dust, and up to 0.27 when significantly soiled with dust (Martin and Ruiz 2005). Soiling of PV panels also causes partial shading, and these

two effects can result in annual power losses of between 5 – 17% (Vidyanandan 2017). Shown below in Figure 13 is the impact of different amounts of different types of dust on the reduction of solar irradiance and its corresponding effect on PV panel power production.

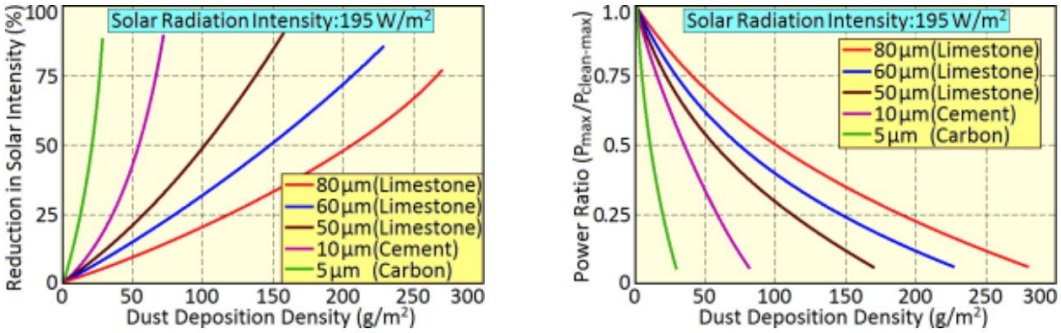

Figure 13. Impact of dust density on solar radiation & PV output.

Source: Reproduced from (Vidyanandan 2017).

The rate of accumulation of dust tends to be higher near the ground and near highways (Vidyanandan 2017).

2.2.4 PV Panel Temperature

As the temperature of PV cells within a module increases, the short circuit current increases, the open circuit voltage decreases and the overall power decreases. The temperature of PV modules increases with increasing irradiance and ambient air temperature; however, it decreases with increasing speed of wind flowing over it (Vidyanandan 2017). The typical change in short circuit current, open circuit voltage, module power and efficiency, normalised against irradiance, with respect to temperature, for silicon PV cells is shown in Figure 14 below.

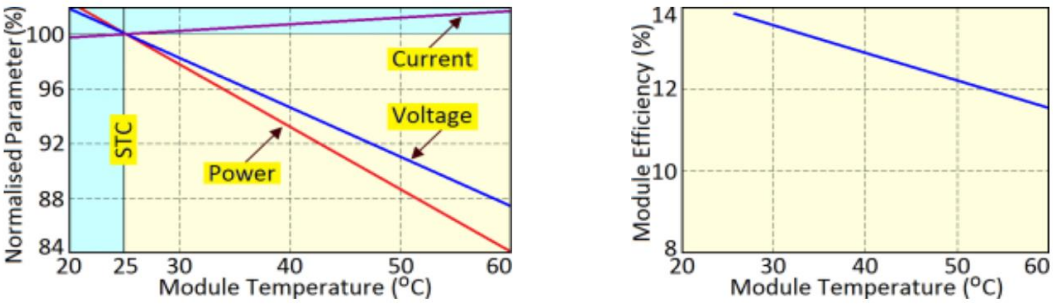

Figure 14. Impacts of temperature on PV cell performance.

Source: Reproduced from (Vidyanandan 2017).

The open circuit voltage tends to decrease by between 0.1V and 0.3V for each degree K increase in temperature while the short circuit current increases by between 2.3 and 4mA/K (Vidyanandan 2017). With the open circuit voltage decreasing more rapidly than the short circuit current increases, the power output decreases. This rate of decrease is approximately 0.4 to 0.5% per degree C increase in module temperature. The current-voltage curve and power-voltage curve of a 240 Wp (peak power) PV module varying with temperature is shown to illustrate these relationships in Figure 15 below.

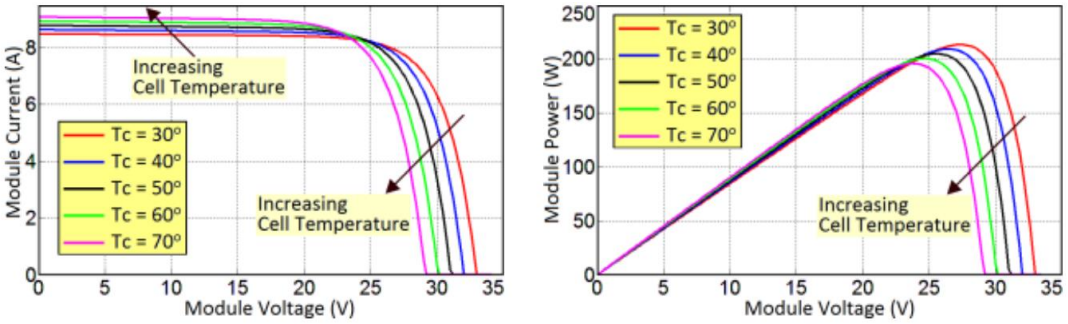

Figure 15. Impact of cell temperature on the I-V and P-V characteristics of a 240 Wp PV module.

Source: Reproduced from (Vidyanandan 2017).

2.2.5 Shading

Modules are comprised of many PV cells connected in series, as shown in Figure 16 below, with each cell typically being modelled as a photo-current source in parallel with a diode, a shunt resistance and a series resistance as shown in Figure 17 below.

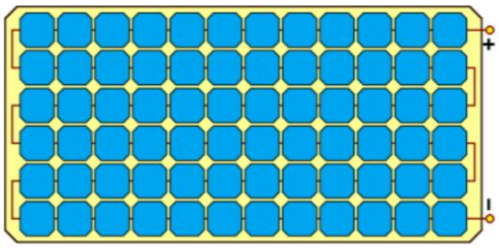

Figure 16. A 72-cell crystalline PV module.

Source: Reproduced from (Vidyanandan 2017).

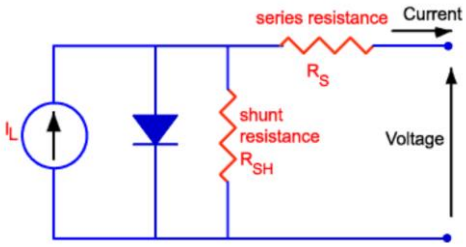

Figure 17. Parasitic series and shunt resistances in a solar cell circuit.

Source: Reproduced from (Honsberg and Bowden n.d.).

The series resistance is caused by the combined internal resistance of the PV cell and its various contacts, while the shunt resistance (sometimes referred to as parallel resistance) is caused by manufacturing defects. The series resistance tends to be small enough to be ignored in calculations generally, while the shunt resistance is very important. During normal operation where every PV cell in a module has enough irradiance such that the diode in the equivalent circuit is conducting, the shunt resistance only causes a small drop in current. This is because the shunt resistance offers an alternative path for current to flow other than the junction of the PV cell. This becomes extremely detrimental in low light conditions when the diode does not have enough current flowing through it and stops conducting. At this time, the current generated by other PV cells connected in series can only flow through the shunt resistor as the leakage current of diodes is generally on the order of 10^{-12}A. The power dissipation is modelled by Equation 21 below.

$$P = I^2R \tag{21}$$

'P' is the power dissipated as heat (W), 'I' is the current (A), and 'R' is the resistance (**Ω**). For very high resistances, which the shunt resistance of a PV cell typically is, the power dissipation as heat increases linearly. However, with more series connected cells, and hence more current, the power dissipation as heat increases quadratically. The compound effect of shaded cells on a PV module is that the overall current and voltage both drop and depending on the amount of current flowing and the shunt resistance, those shaded cells can become very hot and cause damage to the PV module. The equivalent circuit of series connected cells with one cell shaded and the corresponding I-V curve is shown in Figures 18 and 19 below.

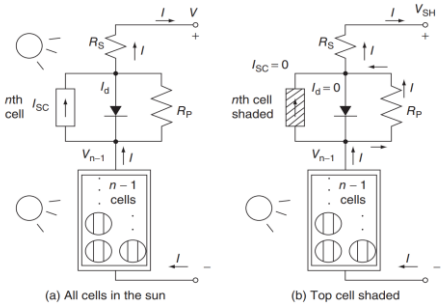

Figure 18. A module with n cells in which all of the cells are in the sun (a) or in which the top cell is completely shaded (b).
Source: Figure reproduced from (Masters 2013).

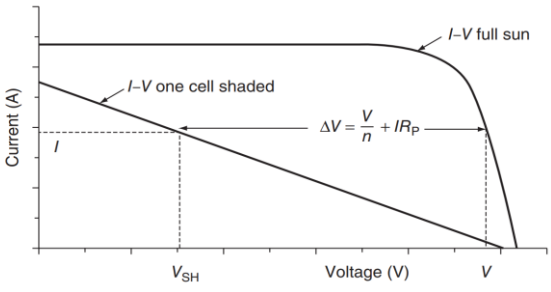

Figure 19. Effect of shading one cell in an n-cell module. At any given current, module voltage drops from V to ΔV.

Source: Reproduced from (Masters 2013).

The effect of uniformly distributed dirt on a PV module, as well as the effect of partial shading of a single cell, and full shading of two cells is shown in Figures 20 and 21 below.

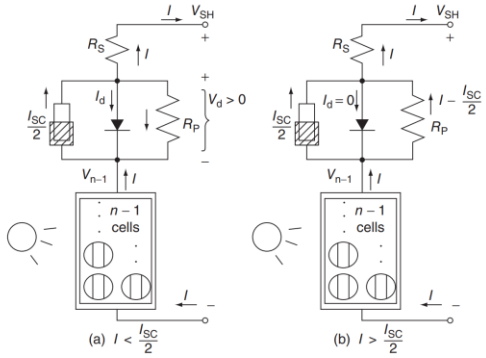

Figure 20. With one cell half-shaded, its equivalent circuit diode still conducts as long as current I from the rest of the module is less than $I_{SC}/2$ (a). Once I exceeds $I_{SC}/2$, the diode shuts off and I passes through R_P and R_S, which can result in very large voltage drops in that cell (b).
Source: Figure reproduced from (Masters 2013).

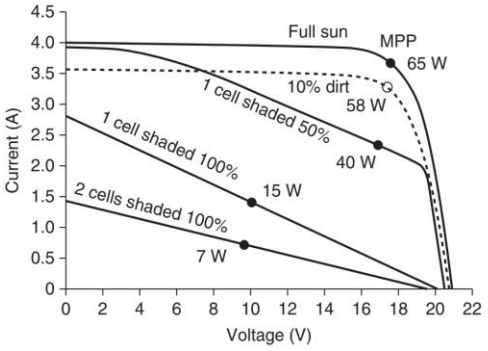

Figure 21. Showing the difference in I–V curves for individual cells being shaded and also for uniformly distributed dirt (dashed) on a module. The dots show power at the MPPs.

Source: Figure reproduced from (Masters 2013).

Most modern PV modules include bypass diodes that allow current to flow through a string of series connected PV cells if one or more cells in that string become shaded which reduces the impact on the I-V curve as shown in Figures 22 and 23 below.

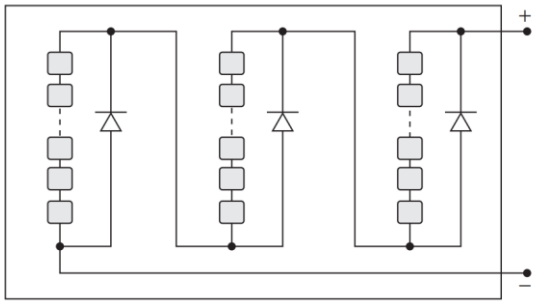

Figure 22. Three bypass diodes, each covering one-third of the cells in a module.

Source: Reproduced from (Masters 2013).

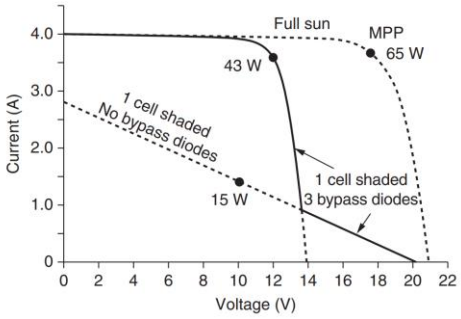

Figure 23. A module with three bypass diodes with one cell shaded. Without the diodes only 15 W would be generated compared to the 43 W provided with diodes.
Source: Reproduced from (Masters 2013).

The bypass diodes do cause a voltage drop of typically 0.5 – 0.6V but this is much less than the voltage drop experienced without their use when current can only flow through the shunt resistance of shaded cells.

2.2.6 Photovoltaic Material

Different photovoltaic materials have different properties but there are generally three types of photovoltaic materials used in most commercially available PV panels. These include monocrystalline silicon, polycrystalline silicon and thin-film photovoltaics including amorphous silicon among others. Their key properties in general and comparisons between these different PV technologies is shown in Table 2 below.

Table 2: Comparison of Common PV Technologies

	Mono-Si	Poly-Si	Thin Film
Efficiency	Most efficient (18 - 22%)	Less efficient (14 - 18%)	Least efficient (10 - 12%)
Manufacturing	From single Si crystal	By fusing Si crystals	Many layers of PV material
Suitable for	Standard temperature	Moderately high temp.	High temp.
Area need/kW	Least	Less	Large
Energy yield per unit area	Hi due to high Si content	Hi due to high Si content	Lo due to low Si content
Performance at low light	Low	Low	Moderate
Gap between Voc and Vmp	15 - 20% (less is better)	15 - 20%	22 – 28%
Temperature Coefficients	High	High	Low (Lo is better)
Fill-factor	70 - 80% (Hi is better)	70 - 80%	60 - 68%

Source: Table reproduced from (Vidyanandan 2017).

2.2.7 Panel Degradation

Most manufactures provide a 25-year warranty on their PV panels with an expected loss of maximum power generation of 10% in the first 10 years followed by a further 10% loss in 10 – 15 years as shown in Figure 24 below. The standard rates of power loss for different technologies are also shown in Table 3 below.

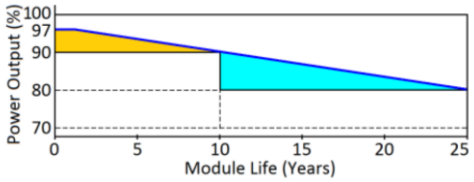

Figure 24. Life span of a typical solar PV module.

Source: Reproduced from (Vidyanandan 2017).

Table 3: Average Yearly Output Loss of PV Cells

PV Cell Type	Output loss (%/year)
Monocrystalline Silicon (mono-Si)	0.36
Cadmium Telluride (CdTe)	0.4
Polycrystalline Silicon (poly-Si)	0.64
Amorphous Silicon (a-Si)	0.87
Copper Indium Gallium Selenide (CIGS)	0.96

Source: Table reproduced from (Vidyanandan 2017).

2.2.8 Overall Module Energy Conversion Efficiency

Most PV modules have the short circuit current (I_{SC},) open circuit voltage (V_{OC}), maximum power current (I_{mp}), maximum power voltage (V_{mp}), maximum power (P_{max}) and module efficiency (μ_m) values given under standard testing conditions (STC). Standard testing conditions include an irradiance of 1000W/m^2 (with an angle of incidence of 0°), module temperature of 25°C, and an air mass index of 1.5. The temperature coefficients of these parameters are also given at STC, however there is often a nominal operating cell temperature (NOCT) value provided as well. NOCT testing conditions include an irradiance of 800W/m^2 (with an angle of incidence of 0°), ambient temperature of 20°C and wind speed of 1m/s, with the reason being that this is more representative of typical operating conditions in the field. To calculate the actual cell temperature in a PV module, the NOCT value and actual irradiance incident upon the module are used as shown in Equation 22 below (Masters 2013).

$$T_{cell} = T_{amb} + \left(\frac{NOCT - 20°C}{0.8kW/m^2}\right) \cdot S(kW/m^2) \quad (22)$$

'T_{cell}' is the temperature of the cell (°C), 'T_{amb}' is the ambient temperature (°C), 'S' is the measured total irradiance incident upon the module, shown here in kW/m^2. The inclusion of 0.8kW/m^2 in the denominator is to account for the testing conditions of NOCT. Using the temperature coefficients of short circuit current (α_I), open circuit voltage (α_v) and maximum power (α_p), the corresponding short circuit current, open circuit voltage and maximum power can be closely approximated using Equations 23 – 25 below (Masters 2013).

$$I_{sc} = I_{sc,STC}[1 + \alpha_I(T_{cell} - 25)] \times S \quad (23)$$

$$V_{oc} = V_{oc,STC}[1 + \alpha_v(T_{cell} - 25)] \quad (24)$$

$$P_{mp} = P_{mp,STC}\left[1 + \alpha_p(T_{cell} - 25)\right] \times S \quad (25)$$

'$I_{sc,STC}$' is the short circuit current given at STC (A), '$V_{oc,STC}$' is the open circuit voltage given at STC, and '$P_{mp,STC}$' is the maximum power given at STC. Note the exclusion of irradiance in the calculation of the open circuit voltage, which is due to the fact that the open circuit voltage does not change much at all with irradiance. Using the calculated maximum power at a given temperature and irradiance, the effective solar energy conversion efficiency of the module (μ_{pv}) can be calculated with Equation 26 below (Masters 2013).

$$\mu_{pv} = \frac{P_{mp}}{S \times A} \quad (26)$$

'A' is the overall area of the module (m^2). The overall module solar energy conversion efficiency will always be slightly lower than the efficiency of the PV cells that comprise it due to the unproductive areas of the module i.e., the space between PV cells, frame etc. All other effects previously mentioned are incorporated by this final efficiency calculation, for example the effect of angular loss is accounted for by the total irradiance 'S', as is the cosine effect, cloud cover etc, while the effect due to temperature is accounted for in the calculation of the maximum power.

2.3 Previous Research of Two-Axis Sun-Tracking Performance and Vehicle Integrated Photovoltaics

2.3.1 Two-Axis Sun-Tracker Performance

A study compared the performance of PV panels with fixed tilt (equal to latitude angle), single-axis tracking (tilt angle of 40°, azimuth tracking), and two-axis tracking as a function of both total irradiance, and direct beam irradiance fraction (Logan and Raichle n.d.). The findings were that the average power produced by the two-axis tracking PV panel was 25% greater than the average power produced by the fixed-axis panel, while the average power produced by the single-axis tracking PV panel was 16% greater than that of the fixed-axis panel. This was when the total irradiance incident upon the panels was considered, however when the direct beam irradiance fraction was considered, a non-linear trend was observed as shown in Figure 25 below.

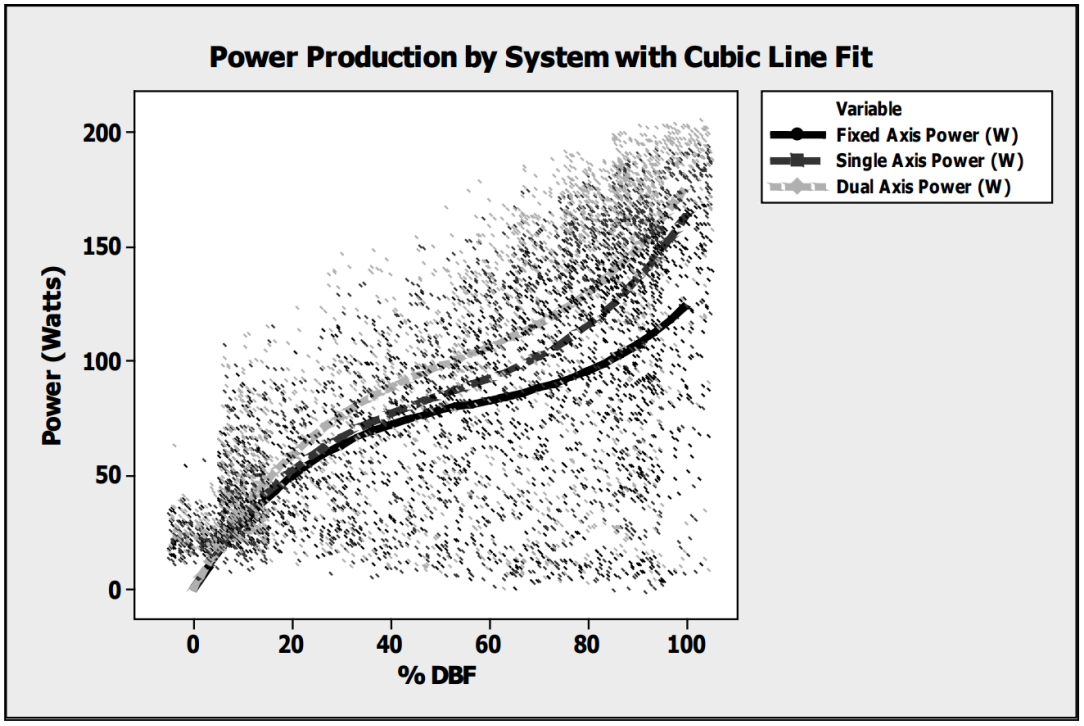

Figure 25. Relationship between power and direct beam fraction for all measured irradiance levels.

Source: Reproduced from (Logan and Raichle n.d.).

The study suggests that as the direct beam fraction of irradiance increases to 100% of the total irradiance that there is a greater variation between the power generated by two-axis tracking, single-axis tracking and fixed-tilt PV panels. The implication of this is that when diffuse or reflected light represent more significant proportions of the total irradiance, the difference in power production between the different configurations decreases.

Another study found that a two-axis tracking PV system generated 30.79% more energy over the course of a year compared with a fixed-tilt (tilt angle equal to latitude angle) system (Eke and Senturk 2012). The power distribution with time for a representative day in Summer and Winter at the site is shown in Figure 26 below.

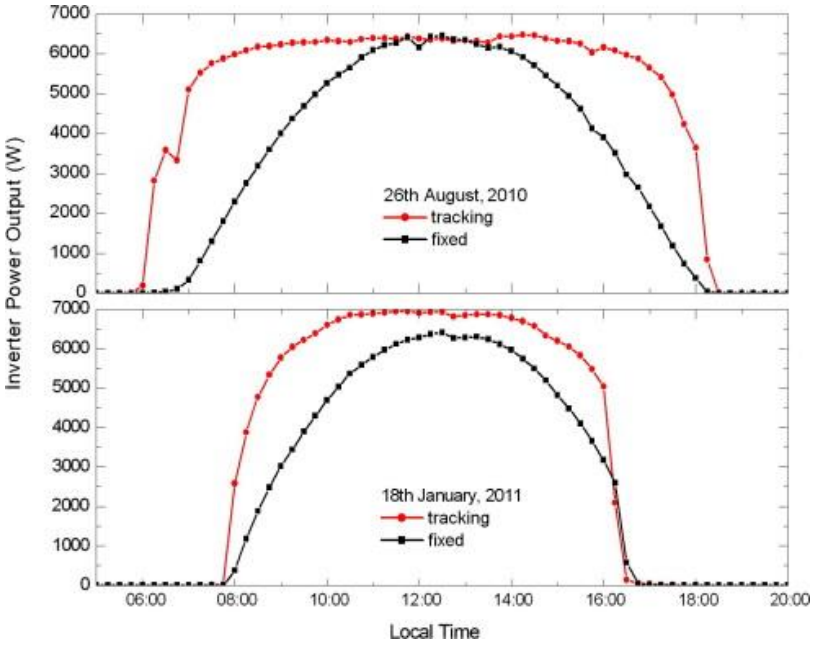

Figure 26. PV systems operation in representative days.

Source: Reproduced from (Eke and Senturk 2012).

The maximum gain in energetic performance of the two-axis system was found to be 42.5% in the month of June (Summer) and the minimum was 17% in January (Winter). The temperature of the modules of the two systems in representative days of the year are shown in Figure 27 below.

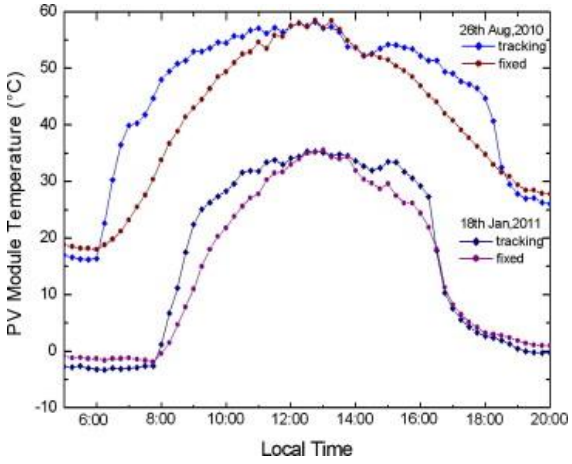

Figure 27. Temperature variation of PV modules for representative days.

Source: Reproduced from (Eke and Senturk 2012).

The maximum temperature of the two-axis system was found to be 58.5°C while the maximum temperature of the fixed-tilt system was 35.6°C.

Another study assessed the impact of rotation and translation on a fixed-tilt PV module (tilt angle of 25°) and a two-axis tracking PV module in three scenarios (Wu, Wang and Chang n.d.):

- Both systems stationary at the same location.
- Rotating by 360° about the zenith (30° at a time) at a fixed location.
- On a slow moving (1km/h) mobile platform.

The study found that when both systems were at the same location, the two-axis tracking system generated on average 35.91% more power than the fixed tilt system with the power distribution shown in Figure 28 at right.

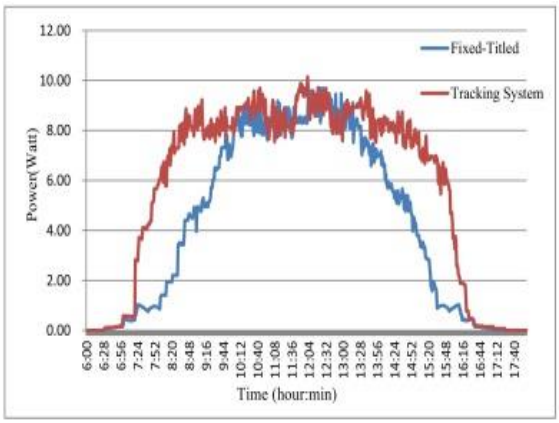

Figure 28. Power generation on mostly clean day for the two systems at fixed location.
Source: Reproduced from (Wu, Wang and Chang n.d.).

In the second scenario both systems were rotated in increments of 30° at noon and left in that rotation for five minutes at a time, until a full 360° of rotation was recorded. The findings were that the two-axis tracking system generated on average 60% more power than the fixed-tilt system. The power generation with respect to heading angle is shown in Figure 29 at right.

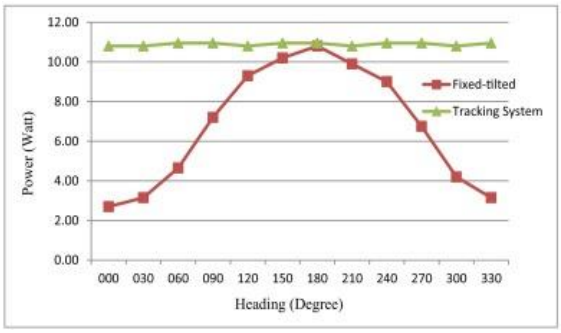

Figure 29. Power generation by the two systems rotation in 360 degrees, respectively.
Source: Reproduced from (Wu, Wang and Chang n.d.).

Lastly, when moving the two systems on a mobile platform the average gain in power production was 113.5% with the power distribution over the testing time, plotted against the heading shown in Figure 30 at right.

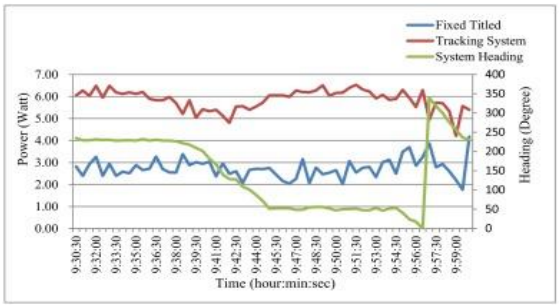

Figure 30. Power generation by the two systems on mobile platform, respectively.
Source: Reproduced from (Wu, Wang and Chang n.d.).

2.3.2 Irradiance Incident Upon Vehicles

A study focussed on measuring the incident irradiance on different parts of a vehicle proposed a mobile pyranometer array (MPPA) attached to the roof of a car as shown in Figure 31 below (Ota, et al. 2019).

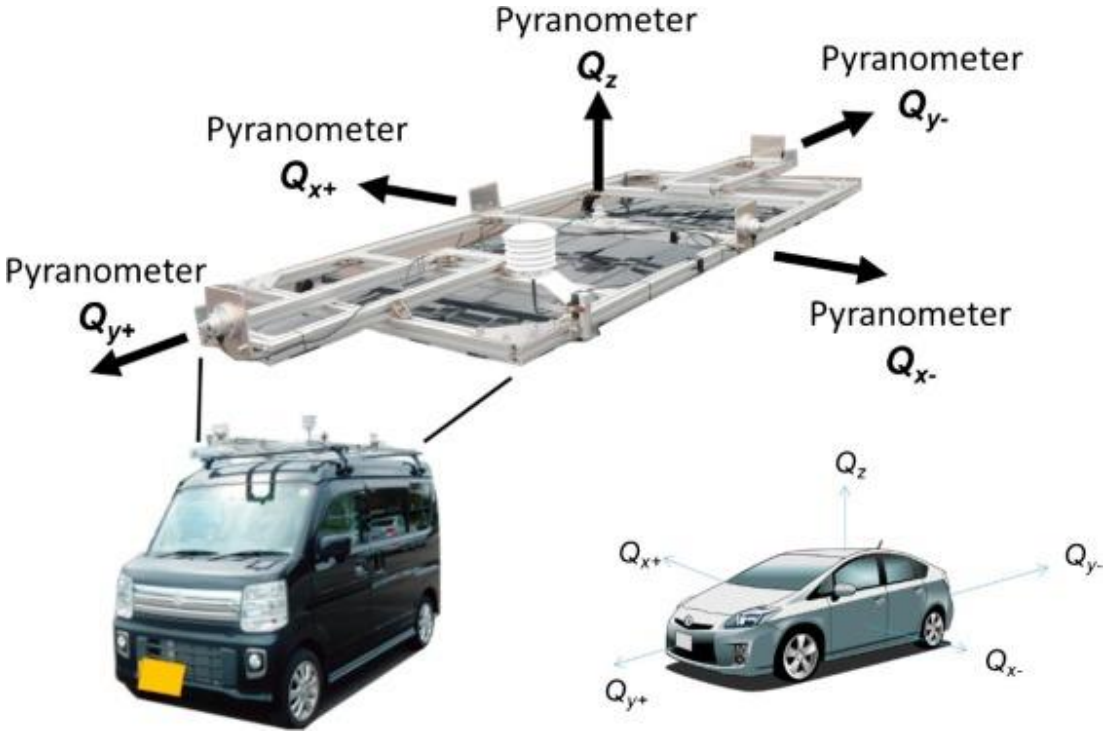

Figure 31. Mobile multiple pyranometers array for a vehicle.

Source: Reproduced from (Ota, et al. 2019).

The car was parked in a parking lot with the front pointing approximately North resulting in the data shown in Figure 32 at right being obtained for the irradiance detected by each pyranometer.

The distribution of irradiance with respect to time of day on the roof of the car was found to be similar to that of the global horizontal irradiance distribution.

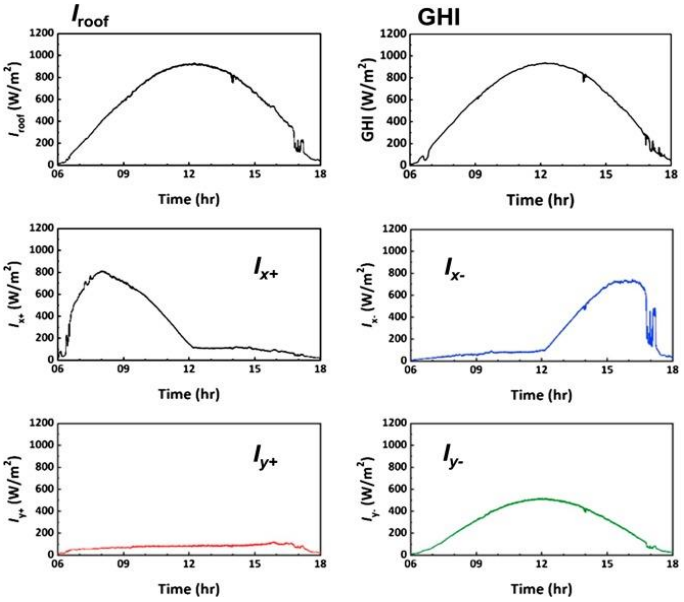

Figure 32. Global irradiances for Ix+, Ix−, Iy+, Iy−, and Iroof measured by MMPA on a clear sunny day. GHI measured by the horizontal pyranometer under a static irradiance measurement system is also shown.
Source: Reproduced from (Ota, et al. 2019).

Another study also made use of an MPPA and recorded irradiance data over the course of a year of driving approximately the same route shown in Figure 33 below (Araki, Ota and Yamaguchi 2020).

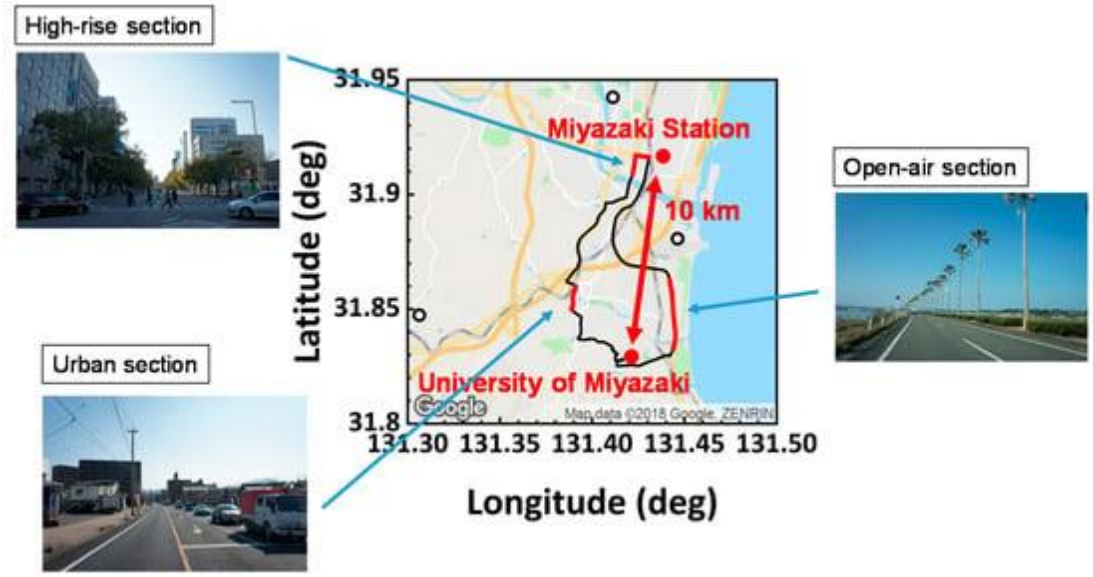

Figure 33. Most frequent driving course of the dynamic solar irradiance measurement in the car.

Source: Reproduced from (Araki, Ota and Yamaguchi 2020).

The typical driving route was traversed between 11:30am and 12:30pm with the typical irradiance compared against a horizontal pyranometer measuring the GHI at the University of Miyazaki as shown in Figure 34 below.

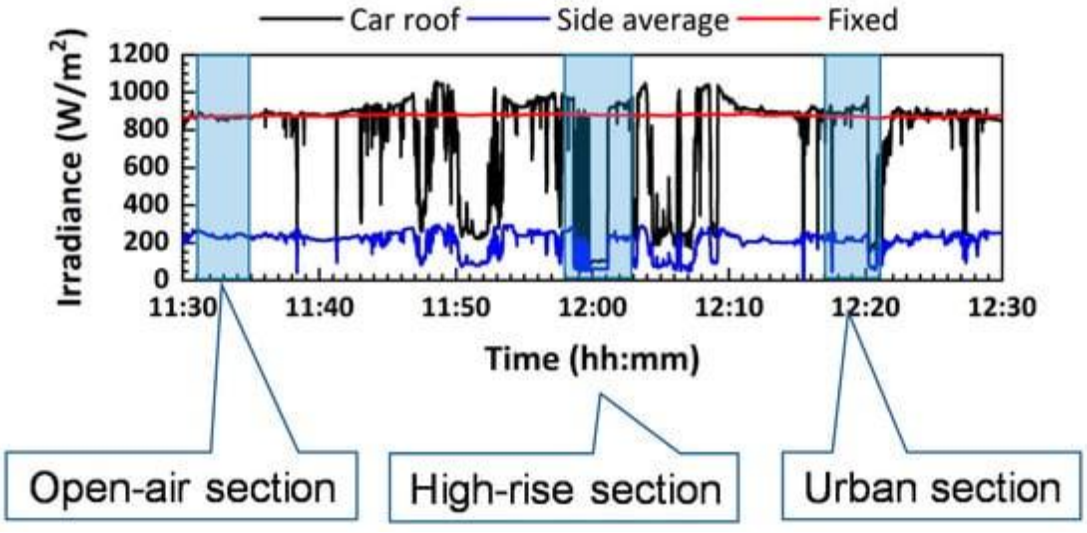

Figure 34. Monitored the result of the solar irradiance on the car roof and car sides in the driving route.

Source: Reproduced from (Araki, Ota and Yamaguchi 2020).

The irradiance measured on the roof and sides of the car respectively were modelled and compared against the GHI as shown in Figure 35 below.

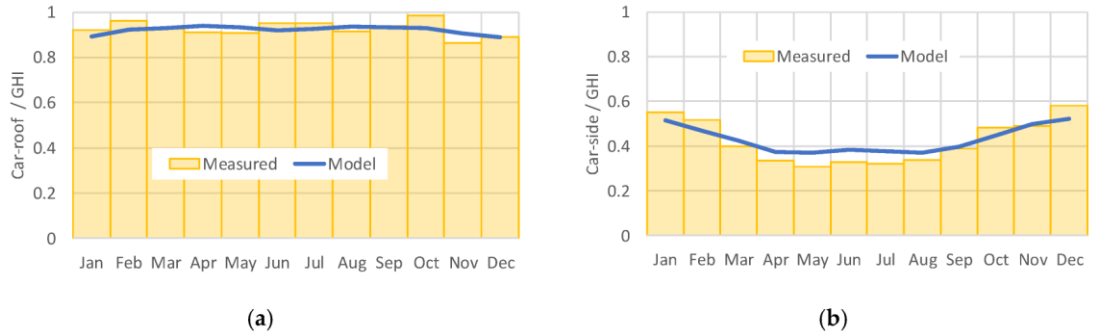

(**a**) (**b**)

Figure 35. Monthly-based comparison between the measured solar irradiance around the car (bar-chart) and modelled (typical year from the METPV-11 solar database, namely, Meteorological Test data for Photovoltaic system) solar irradiance on the car (line-chart): (a) car roof irradiance; (b) car side irradiance.

Source: Reproduced from (Araki, Ota and Yamaguchi 2020).

The main findings are that the roof of the vehicle tends to experience approximately double the irradiance of the sides of the vehicle combined.

2.3.3 Two-Axis Sun-Tracking Systems on Mobile Platforms

A study investigated the improvement in power production of a PV panel using a parallel actuated system to track the Sun in simulation with the actuator system shown in Figure 36 below (Pisanti 2015).

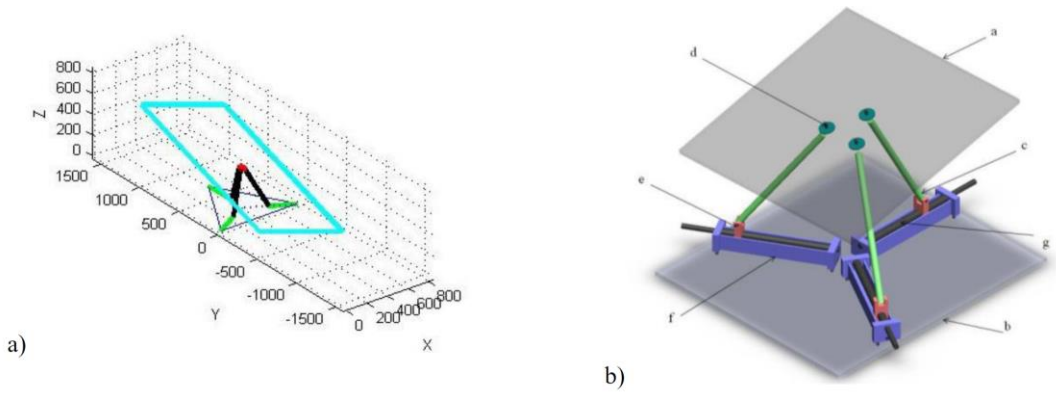

Figure 36. a) Graphical output by the MATLAB model, b) Mobile solar roof prototype 3D modelled

Source: Reproduced from (Pisanti 2015).

The two-axis tracking system was modelled against a horizontal system using data from the PvWATTS database and estimated an average 30% gain in energy production from the two-axis system at lower latitudes, and up to 47% gain at higher latitudes.

2.3.4 Actuation Methods

Generally linear actuators and rotary actuators are used when achieving two-axis Sun-tracking as shown in Figure 37 below (Redekar, Deb and Ozana 2022).

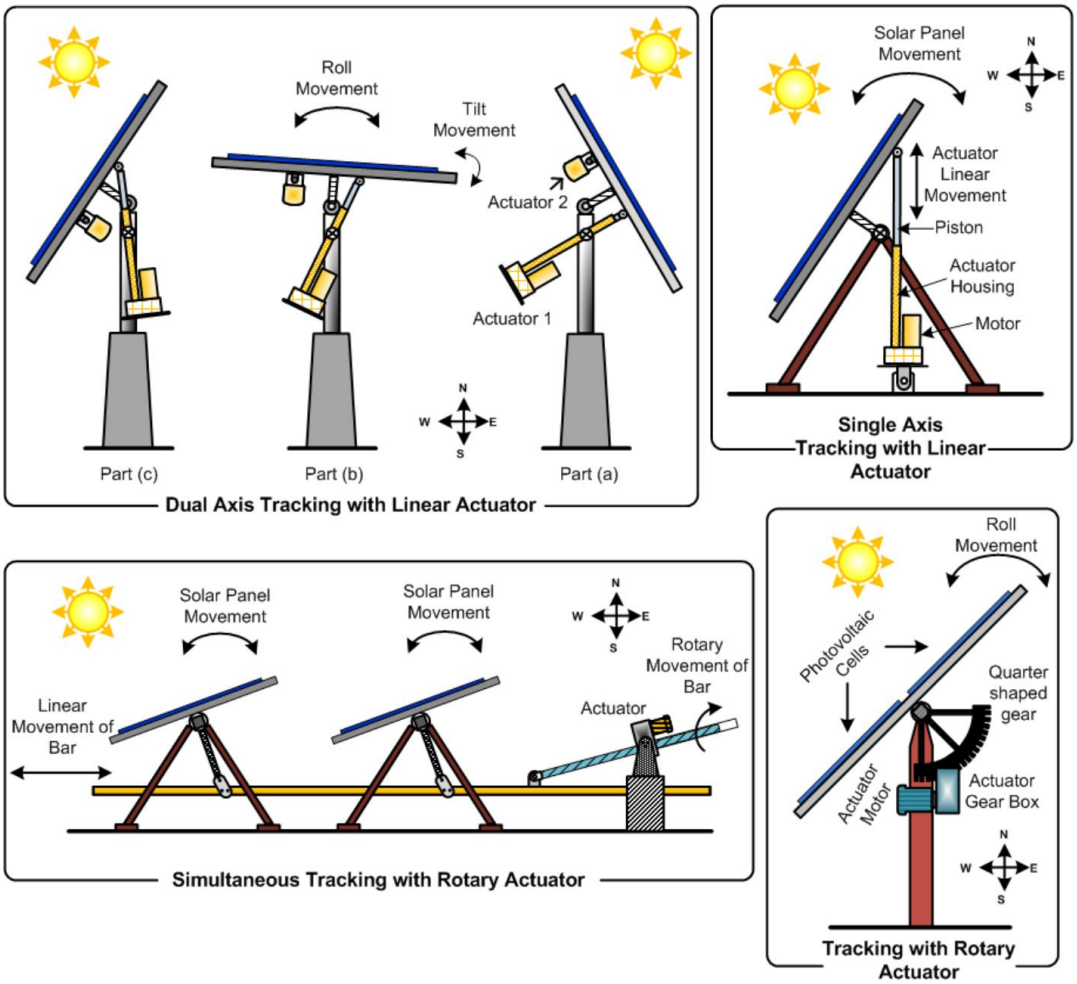

Figure 37. Electric actuators functioning in solar tracking applications.

Source: Reproduced from (Redekar, Deb and Ozana 2022).

However, there is a constraint when it comes to implementing these types of actuation systems on a mobile platform such as a car or truck.

The configuration space of most two-axis Sun-tracking systems is such that the PV panel is raised above the ground plane either directly connected to actuators or to mechanical linkages that are driven by actuators. The consequence of this is that PV panels mounted onto mobile platforms cannot be actuated in the same way as when the PV panel is tilted it would interfere with the plane of the roof of the vehicle. If, however, the PV panel is raised up off the plane of the roof and actuated in the standard way that most PV panels are actuated, or via a parallel actuated system as seen earlier, then this issue is negated.

The problem with this approach, however, is that the PV panel cannot be stowed flat when the vehicle is in transit. This presents a couple of issues, namely the increased aerodynamic drag force, but also the increased stress that the mechanical components supporting the PV panel experience due to wind loading. There appears to be a gap in the literature regarding two-axis Sun-tracking actuation systems for PV panels on mobile platforms.

2.4 Considerations of PV Panels on Locomotive Performance

2.4.1 Net Force Acting on a Vehicle in Rectilinear Motion

The net force acting on a vehicle in rectilinear motion, using Newton's second law of motion, is described in Equation 27 below.

$$F_{net} = F_t - F_f - F_g - F_d = ma \tag{27}$$

Where 'F_{net}' denotes the net resultant force acting on the vehicle, 'F_t' denotes the tractive force exerted by the wheels of the vehicle, 'F_f' denotes the friction force due to rolling resistance between the wheels and the ground, 'F_g' is the gravitational (or slope) force, 'F_d' is the aerodynamic drag force, 'm' denotes the mass of the vehicle (kg), and 'a' denotes the acceleration of the vehicle (m/s^2). These forces are decomposed further in Equations 28.1 – 3 below.

$$F_f = \mu_r mgcos(\theta_i) \tag{28.1}$$

$$F_g = mgsin(\theta_i) \tag{28.2}$$

$$F_d = \frac{1}{2}\rho C_d A v^2 \tag{28.3}$$

Where 'μ_r' denotes the overall coefficient of rolling friction between the points of contact of the vehicle and the ground, 'g' denotes the acceleration due to gravity (m/s^2), 'θ_i' denotes the angle of inclination (or declination) of the ground (degrees), 'ρ' denotes the density of air (kg/m^3), 'C_d' denotes the coefficient of aerodynamic drag of the vehicle, 'A' denotes the cross-sectional area of the vehicle normal to the direction of wind (m^2), and 'v' denotes the relative velocity of the wind (m/s). Equations 28.1 – 3 can be substituted into Equation 27 as shown below in Equation 28.4.

$$F_{net} = F_t - \mu_r mgcos(\theta_i) - mgsin(\theta_i) - \frac{1}{2}\rho C_d A v^2 = ma$$

$$\rightarrow F_{net} = F_t - (mg) \cdot [\, \mu_r cos(\theta_i) + sin(\theta_i) \,] - \frac{1}{2}\rho C_d A v^2 = ma \qquad (28.4)$$

For a vehicle moving at a constant velocity, Newton's first law of motion can be used to find the tractive force from Equation 28.4 as shown in Equation 29 below.

$$F_{net} = F_t - (mg) \cdot [\, \mu_r cos(\theta_i) + sin(\theta_i) \,] - \frac{1}{2}\rho C_d A v^2 = 0$$

$$\rightarrow F_t = (mg) \cdot [\, \mu_r cos(\theta_i) + sin(\theta_i) \,] + \frac{1}{2}\rho C_d A v^2 \qquad (29)$$

2.4.2 Power Requirement of Locomotion

The power required to be delivered to the wheels of a vehicle moving at a constant velocity can be found by substituting the tractive force from Equation 29 into the equation of mechanical power in translation in Equation 30 below.

$$P_t = F_t v \qquad (30)$$

Where 'P_t' is the power delivered to the ground via the wheels (W). The power that must be produced by the propulsion system of a vehicle is greater than that delivered to the wheels due to friction, heat and other energetic losses in the transmission and propulsion system itself. These losses can be aggregated into a single efficiency factor which allows the required power from the propulsion system to be calculated from the tractive power as shown in Equation 31 below.

$$P_p = \frac{P_t}{\eta_p} \qquad (31)$$

Where 'P_p' is the propulsion power (W), and 'η_p' is the efficiency of the power delivery from the propulsion system to the contact point of the wheels and the ground.

2.4.3 Relative Effects of Mass and Aerodynamic Drag

From Equation 29 the tractive force required from the wheels of a vehicle to maintain a constant velocity demonstrates that there is a directly proportional relationship to vehicle mass and cross-sectional area, as well as a square proportionality to velocity. When substituting the expansion of the tractive force from Equation 29 into Equation 30, a cubic proportionality to velocity due to aerodynamic drag is found for tractive power as shown in Equation 32 below.

$$P_t = \left((mg) \cdot \left[\, \mu_r cos(\theta_i) + sin(\theta_i) \,\right] + \frac{1}{2}\rho C_d A v^2\right) \cdot v$$

$$\rightarrow P_t = (mgv) \cdot \left[\, \mu_r cos(\theta_i) + sin(\theta_i) \,\right] + \frac{1}{2}\rho C_d A v^3 \qquad (32)$$

It can be seen that the tractive power requirement due to drag would be significantly greater than that of the mass of the vehicle for higher speeds. The threshold velocity at which point the main component of tractive power becomes the aerodynamic drag component can be found by equating it to the mass component as shown in Equation 32.1 below.

$$(mgv) \cdot \left[\, \mu_r cos(\theta_i) + sin(\theta_i) \,\right] = \frac{1}{2}\rho C_d A v^3$$

$$(mg) \cdot \left[\, \mu_r cos(\theta_i) + sin(\theta_i) \,\right] \cdot \frac{2}{\rho C_d A} = v^2$$

$$\rightarrow v = \sqrt{(mg) \cdot \left[\, \mu_r cos(\theta_i) + sin(\theta_i) \,\right] \cdot \frac{2}{\rho C_d A}} \qquad (32.1)$$

As mass increases, this threshold velocity increases, while as cross-sectional area increases the threshold velocity decreases. In order to minimise the overall tractive power requirement when adding PV panels to a vehicle, more emphasis should be placed on the cross-sectional area that is added to the vehicle rather than the weight of the PV panels being added. This is because the proportion of the total mass of the vehicle that the PV panel contributes is likely to be very small, whereas the proportion of overall cross-sectional area that it can contribute is more significant.

3.0 EXPERIMENTAL PROCEDURE

3.1 Testing Apparatus

3.1.1 PV Panels

Six of the same PV panel with the following stated specifications were used:

- Typical peak power = 0.55W
- Voltage at peak power = 5.5V
- Current at peak power = 100mA
- Length = 70mm
- Width = 55mm
- Efficiency = 17%

3.1.2 Sensors

For each two-axis tracking system four of the same light dependent resistors were used with the following stated specifications:

- Light resistance = 135K – 420K
- Dark resistance = 10MΩ

For each of the six PV panels being tested, the same DS18B20 digital thermometers were used with the following key stated specifications:

- ±0.5°C Accuracy from -10°C to +85°C

3.1.3 Actuators

For each of the two-axis tracking systems, two 28BYJ-48 stepper motors and accompanying ULN2003 driver boards were used with the stated key specifications:

- Speed variation ratio = 64
- Stride angle = 5.625º/64
- Number of phase = 4

It has been inferred that ‘speed variation ratio’ corresponds to gear ratio and that ‘stride angle’ corresponds to step angle. This means that for a full rotation of the output shaft of the stepper motor it has to step through 4096 steps. However, to reduce the number of GPIO pins required by the microcontroller the control signals were inverted for opposite coils causing double steps to be taken resulting in a resolution of 2048 steps per revolution of the output shaft.

3.1.4 Other Components

In order to reduce the number of GPIO pins required by the stepper motors a CD4069UB CMOS hex inverter IC chip was used for both test rigs. To ensure accurate readings of temperature by the DS18B20 sensors, thermal transfer tape was used between the middle of the PV panel and flat edge of the DS18B20 on every PV panel with the following stated specifications:

- Thermal conductivity = 1.4W/m-k
- Thickness = 0.2mm

3.1.4 Microcontroller Unit

For each of the platforms one ESP32 devkit was used. The code is shown in Appendix A.

3.1.5 Measurement Equipment

For illuminance measurements a LX1010/LX1010B+ handheld lux meter was used with the following key specifications on the instrument:

- Cosine response $f_2 < 2\%$.
- Total accuracy for all common light source = ± 11% + 2 digits
- Total accuracy for source A 2586K standard light source = ± 3% rdg + 10 digits

For voltage and current measurements of the PV panels during testing a Digitech QM1326 DMM was used with the following key specifications:

- DC voltage: 400mV, 4V, 40V, 400V, 1000V (±0.5%)
- DC current: 4mA, 40mA, 400mA, 10A (±1.2%)

3.1.6 Flat and Incline Platforms

In order to assess the impact of platform configuration on the power generated by the flat, polar mounted and two-axis tracking PV panels, two platforms were fabricated. One was made such that all the test panels would be resting on a horizontal surface (platform tilt angle = 0º with respect to the ground plane) and the other was made such that the panels would be resting on an incline surface, oriented southward (platform tilt = -20º with respect to the ground plane). The purpose of this was to simulate the effect of a mobile platform on an incline facing South which is the worst possible configuration for a mobile platform South of the equator and outside of the Tropic of Cancer.

3.1.7 3D Printed Mounts

Two identical 3D printed parts were made for the polar mounted PV panels that is a simple triangular frame upon which a PV panels rests on the hypotenuse with a tilt angle of 32º as this is approximately equal to the latitude of the testing location. Two identical 3D printed assemblies of the tracking frame were made to accommodate two stepper motors, the PV panels and their cables.

3.2 Experimental Setup

3.2.1 PV Panel Configurations

On the flat platform there were three PV panels mounted in the following configurations:

1. Flat PV panel: Tilt angle = platform tilt angle, azimuth angle = 0º.
2. Polar mounted PV panel: Tilt angle = 32º, azimuth angle = 0º.
3. Two-axis PV panel: Tilt angle = platform tilt angle = 0º, azimuth angle = 0º.

On the incline platform there were three PV panels mounted in the following configurations:

1. Flat PV panel: Tilt angle = platform tilt angle, azimuth angle = 0º.
2. Polar mounted PV panel: Tilt angle = 32º, azimuth angle = -180º.
3. Two-axis PV panel: Tilt angle = platform tilt angle, azimuth angle = 0º.

Note: the polar mounted PV panel on the incline platform has a tilt angle of 32º but an azimuth angle of -180º with respect to the plane of the incline platform hence the PV panel has a tilt angle of -52º with respect to the ground plane.

3.2.1 Site Location

The site was located in Willetton (lat = 32.0543° S, long = 115.8894° E). Both platforms were mounted via G-clamps to a fence which was approximately normal to the ground i.e., 90º. The platforms were located on a position along the fence such that they had the best view of the Sun throughout the day as there were obstructions such as trees blocking light from before about 9am and after 4pm as seen in Figures 38 and 39 below.

Figure 38. Ryan Coble-Neal, *Horizontal platform (control).* 2023, Digital Image. CC BY-SA 2.0

Figure 39. Ryan Coble-Neal, *Incline platform (experiment).* 2023, Digital Image. CC BY-SA 2.0

3.3 Measurement Procedure

3.3.1 PV Panel Measurements

The following steps were taken when measuring the short circuit current and open circuit voltage of all PV panels across both the flat and incline platforms:

1. Observe the time at the start of the measurement.
2. Place the lux-meter sensor on the PV panel such that it is parallel and resting on the panel and observe the reading (kLUX).
3. Connect the wires of the PV panel to the DMM and measure the open circuit voltage and observe the reading (V).
4. Switch the DMM to measure current and measure the short circuit current and observe the reading (mA).
5. Record the time and the measurement data.

This process typically took less than 30 seconds to complete, however as the day of testing did have some cloud cover there were times where the measurement of illuminance did not correspond to the actual illuminance on the PV panels when measuring their short circuit current and open circuit voltage.

3.3.2 Recording Two-Axis Stepper Angles

During the morning hours (9am to 11:30am) the azimuth steppers for both trackers were initialised such that the attached PV panel was pointing due East, hence the start of their step count began at 0 whilst pointing East. During the rest of the day the azimuth steppers of both trackers were initialised such that the attached PV panel was pointing due North, hence the start of their step count began at 0 whilst pointing North. Both of the elevation (or tilt) steppers were initialised such that the attached PV panel was pointing at a tilt angle of 90º with respect to the plane of the platform upon which they were resting, hence their step counts began at 0 whilst tilted up fully. The reason for these initialisations was to allow the tracking algorithm to

accurately track the Sun. After measuring the illuminance, short circuit current and open circuit voltage of the PV panel on each of the two-axis trackers the step count was recorded directly from the serial monitor on a laptop attached to the microcontroller for each of the trackers.

3.4 Data Analysis

3.4.1 Converting Illuminance Measurements

The measured illuminance values for all readings were converted to estimates of irradiance via a conversion factor of 122 using an engineering rule of thumb (Michael, Johnston and Moreno 2020).

3.4.1 Calculating Angles of Incidence

The following part of the procedure was used for the calculation of angles of incidence of all PV panels as the equations are irrespective of PV panel orientation. All calculations were carried out in an Excel workbook:

1. Equation 1 with n = 157 to find the solar declination angle.
2. Equation 4.1 with n = 157 to calculate the ‘B’ empirical parameter.
3. Equation 4 using the calculated ‘B’ parameter to find the equation of time.
4. Equation 3.1 using the calculated equation of time, local longitude = 115.8894° E, local time meridian = 120° E (UTC +8) and the recorded clock time to find the solar time.
5. Equation 2 using the calculated solar time to find the hour angle.
8. Equation 5 with latitude = -32.0543° S, using the calculated hour angle and solar declination angle, then taking the inverse sine to find the elevation angle.
9. Equation 6 using the calculated solar declination angle, hour angle, and elevation angle, then taking the inverse sine to find the two possible azimuth angles.

10. Equation 6.1 using the calculated solar declination angle and latitude angle, then taking the inverse cosine and checking the inequality to find the correct azimuth angle.

The rest of the procedure to calculate the angle of incidence for each PV panel is dependent on the individual configuration angles of the PV panels:

11. Equation 8, taking the inverse cosine with:
    a. Flat mounted PV panel on flat platform:
        i. Panel azimuth = 0º,
        ii. panel tilt = 0º.
    b. Polar mounted PV panel on flat platform:
        i. Panel azimuth = 0º,
        ii. panel tilt = +32º.
    c. Two-axis tracked PV panel on flat platform:
        i. When 0 point = East (+90º):
            1. Panel azimuth = 90º - |(StepCount2 / 2048) * 360º|.
        ii. When 0 point = North (0º):
            1. Panel azimuth = 0º - |(StepCount2 / 2048) * 360º|.
        iii. Panel tilt = 90º - |(StepCount1 / 2048) * 360º|
    d. Flat mounted PV panel on incline platform:
        i. Panel azimuth = 0º,
        ii. panel tilt = -20º
    e. Polar mounted PV panel on incline platform:
        i. Panel azimuth = -180º,
        ii. panel tilt = -52º (from -20º platform tilt angle added to -32º tilt angle facing Southward).
    f. Two-axis tracked PV panel on incline platform:
        i. When 0 point = East (+90º):
            1. Panel azimuth = 90º - |(StepCount2 / 2048) * 360º|.
        ii. When 0 point = North (0º):
            1. Panel azimuth = 0º - |(StepCount2 / 2048) * 360º|.
        iii. Panel tilt = (90º - 20º) - |(StepCount1 / 2048) * 360º|

3.4.2 Calculating Two-Axis Tracker Error

The tracking error of both trackers is calculated by dividing the calculated angles of incidence by 90º, then multiplying by 100%, i.e., 90º is the maximum value of angle of incidence at which point the error is 100%.

4.0 RESULTS AND DISCUSSION

4.1 Initial Theoretical Solar Model Irradiance Data

4.1.1 Simplifying Assumptions

Using Equations 1, 2, 3.1, 4, 4.1, 5, 6 - 19, a simple solar model was created in an Excel workbook making use of the following simplifying assumptions:

- Cloud cover is assumed to be accounted for by the diffuse sky factor and optical depth parameters.
- The value of reflectance of the surrounding environment was pessimistically assumed to be 0.1 at all times.
- Shading is not accounted for as it is highly context specific, so instead it has been assumed that the site is devoid of obstructions and has clear access to direct irradiance at all times.

4.1.2 Base Case Solar Insolation Data

With these simplifying assumptions a base case was modelled at a latitude of -32° that calculates the expected daily insolation values for horizontal, polar mounted and two-axis tracking surfaces. Table 4 below shows the total daily insolation for each of these cases on the 21st day of each month of the year to approximate the average monthly insolation for each configuration.

Table 4: Total daily insolation for horizontal, polar and two-axis tracking surfaces ($kWh/m^2/day$) for the 21^{st} day of each month.

Month	Horizontal	Polar	2-Axis
Jan	9.09	8.01	12.82
Feb	8.02	8.02	11.68
Mar	6.56	7.58	10.08
Apr	4.81	6.50	8.32
May	3.55	5.37	6.77

Jun	3.06	4.84	6.15
Jul	3.45	5.19	6.53
Aug	4.66	6.24	7.90
Sep	6.36	7.32	9.61
Oct	7.91	7.86	11.31
Nov	9.02	7.93	12.59
Dec	9.40	7.91	13.04

From this data the total daily insolation for an average day throughout the year for each case was found. Table 5 shows the average daily insolation for these cases.

Table 5: Average total daily insolation for horizontal, polar and two-axis tracking surfaces ($kWh/m^2/day$)

	Horizontal	**Polar**	**2-Axis**
Average	6.32	6.90	9.73

The relative percentage difference in average total daily insolation for these four cases is given in Table 6.

Table 6: Relative percentage difference in average total daily insolation for horizontal, polar, azimuthal tracking and two-axis tracking surfaces (%)

	Horizontal	**Polar**	**2-Axis**
Horizontal	-	-8.41	-35.05
Polar	+8.41	-	-29.08
1-Axis	+28.99	+22.47	-8.53
2-Axis	+35.05	+29.08	-

The conclusions that can be drawn from the findings of this rudimentary model are that there is at most 35.05% more energy available to an ideal two-axis tracking surface compared with a horizontal surface.

4.2 Experimental Irradiance Data

Due to obstructions causing shading of the experimentation area the data was recorded from 9am to just after 3pm. The total irradiance values incident upon each of the PV modules is shown over the course of the day in Figure 40 below.

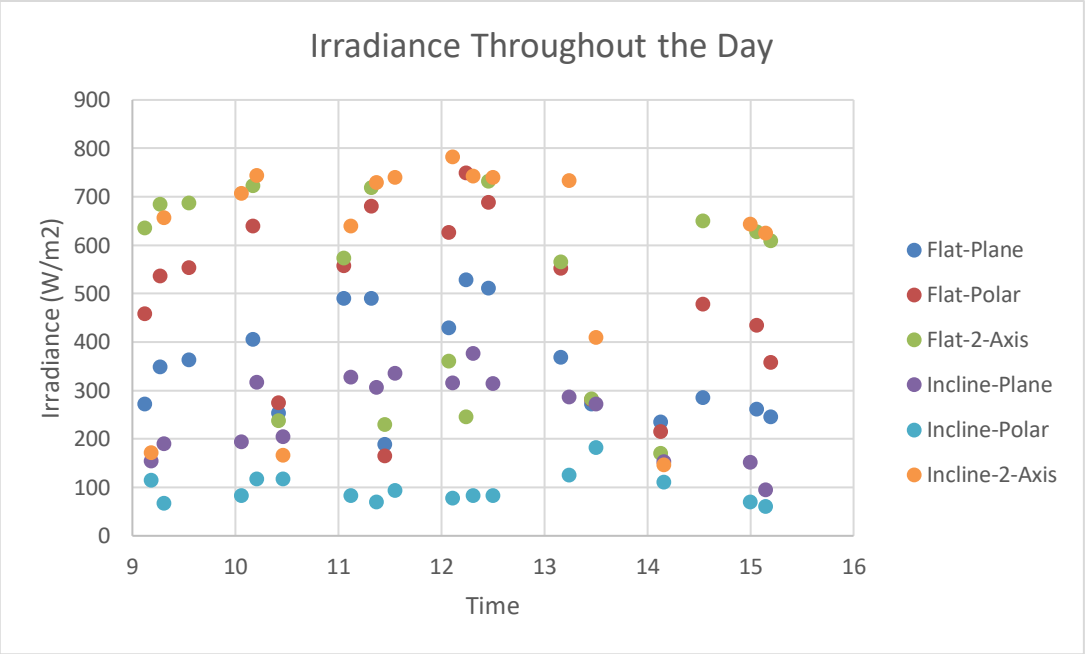

Figure 40. Estimated total incident irradiance on each PV panel.

As seen in the data of the total incident irradiance for each of the PV modules there is a lot of variance between the different configurations. Outliers within trends for each configuration of PV module indicate a time where cloud cover caused more diffuse irradiance. The irradiance as a function of the calculated angle of incidence for each of the times and PV module configurations is shown in Figure 41 below with a cosine curve superimposed.

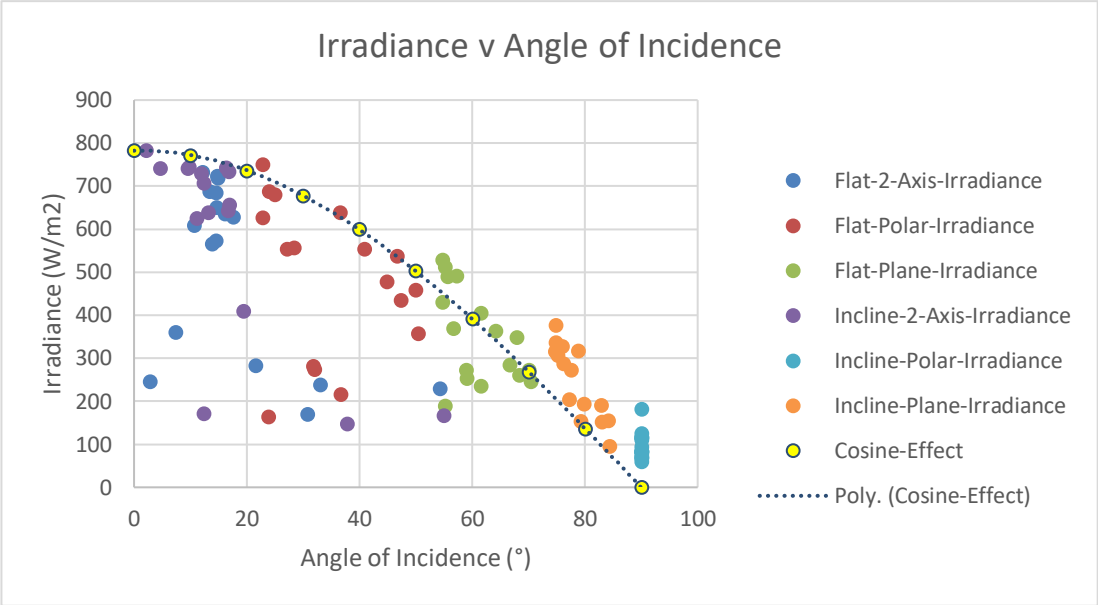

Figure 41. Estimated total incident irradiance on each PV panel plotted against angle of incidence.

The short circuit current of each of the PV modules as a function of angle of incidence is shown in Figure 42 below, also with a cosine curve superimposed.

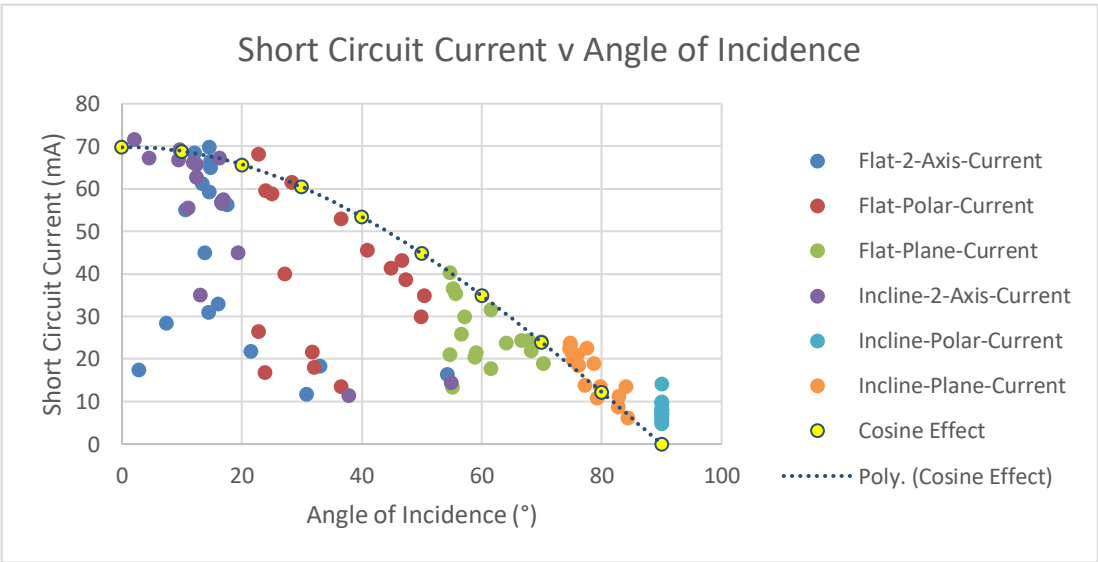

Figure 42. Measured short circuit current of each PV panel plotted against angle of incidence.

The temperature of each PV module as a function of angle of incidence is shown below in Figure 43.

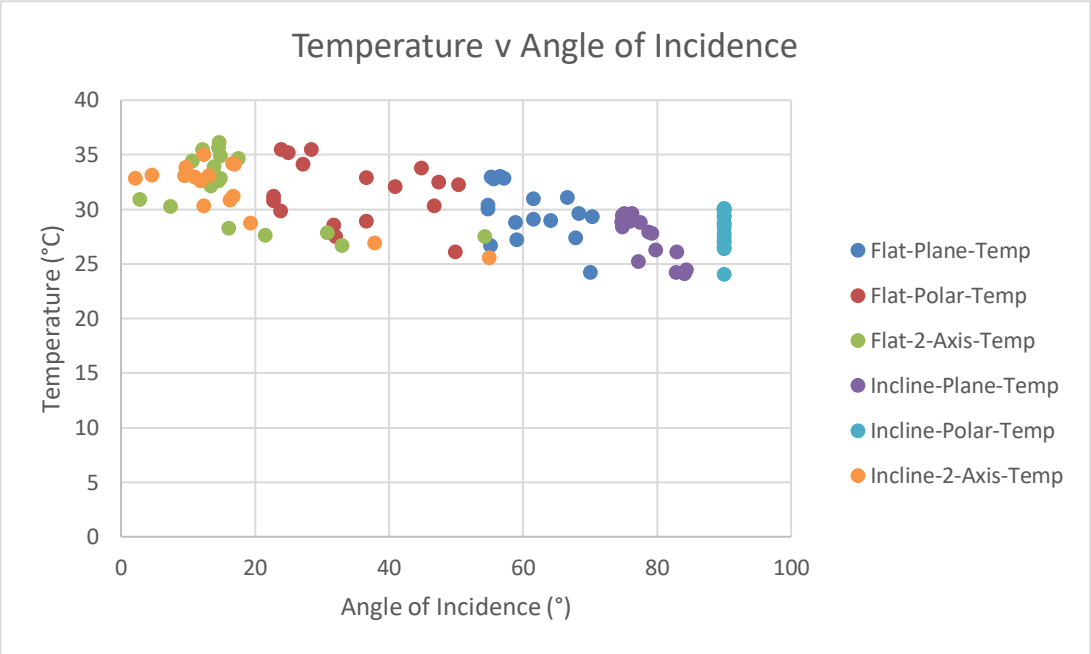

Figure 43. Measured temperature of each PV panel plotted against angle of incidence.

The short circuit current as a function of irradiance is shown in Figure 44 below.

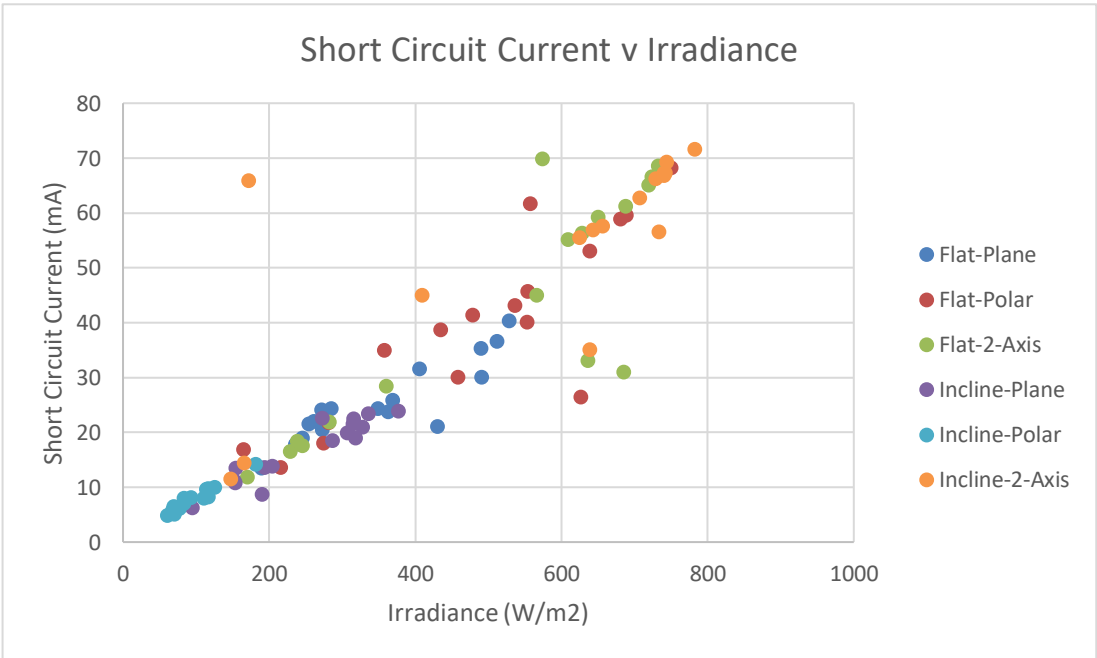

Figure 44. Measured short circuit current of each PV panel plotted against estimated irradiance.

The average tracking error as calculated against the predicted angle of incidence is 20.05% and 18.44% for the two-axis tracker on the flat platform and the two-axis tracker on the incline platform respectively. The average short circuit current of each of the PV modules is shown in Table 7 below.

Table 7: Average Current of Different Configurations of PV Modules

Flat-Plane (mA)	**Flat-Polar (mA)**	**Flat-2-Axis (mA)**	**Incline-Plane (mA)**	**Incline-Polar (mA)**	**Incline 2-Axis (mA)**
25.35	39.48	42.64	16.84	7.8	54.31

From the experimental data the trend in total incident irradiance generally follows a cosine curve with respect to the angle of incidence. The short circuit current is also observed generally following a cosine curve with respect to angle of incidence. The temperature is observed tending to decrease with increasing angle of incidence. The short circuit current is observed to increase linearly with increasing irradiance. The difference in average current produced by the two-axis PV module compared with the flat PV module for the flat platform and inclined platform respectively are 40.54% and 68.99% respectively. The difference between average short circuit current of the two-axis PV module and the polar PV module on the incline platform is 85.64%.

5.0 CONCLUSIONS

The factors that influence the power generation of a PV panel were identified. The expected solar irradiance at a given site was determined with a theoretical solar model and found a maximum increase in energetic potential of 35.05% if two-axis tracking was used compared to a horizontal surface. The most profound impact on the performance of PV panels on mobile platforms was shown to be the angle of incidence between the normal of the PV panel and the direction of beam irradiance through experimentation. The maximum increase in short circuit current by using two-axis tracking was found to be 85.64%. The governing equations that determine the impact of a PV panel on the performance of a mobile platform were found with the impact of additional cross-sectional area being more significant than the mass of the PV panel. A gap in the literature regarding methods of actuation of PV panels on mobile platforms was discovered.

6.0 FUTURE WORK

The original experimental design made use of a digital potentiometer to vary the load connected to each PV panel as well as a multiplexer to switch which panel was connected to this load. The purpose of this was to electronically sweep the I-V curves of all the PV panels. Unfortunately, there was an issue with a non-linearity between the control signal sent by the ESP32 and the resistance generated by the potentiometer which was likely to be an issue with GPIO pins of the ESP32. An MQTT server was also originally going to be used to transfer data from the ESP32 boards to a laptop to then insert into an SQLite database however there was another issue that caused the ESP32 boards to lose connection and become unable to recover. For future work it is recommended that a dedicated voltage and current sensor be used to ensure that voltage and current readings can be taken quickly to avoid the effects of changing irradiance due to cloud cover. Additionally, the methods of actuation of two-axis PV panels on mobile platforms should be explored further as there appears to be a significant gap in the literature regarding a feasible design of such actuation.

7.0 REFERENCES

Araki, Kenji, Yasuyuki Ota, and Masafumi Yamaguchi. 2020. “Measurement and Modeling of 3D Solar Irradiance for Vehicle-Integrated Photovoltaic.” *Applied Sciences.*

Australian Broadcasting Corporation. 2021. *Van life movement gains popularity as people want to live cheaply with the best views.* Australian Broadcasting Corporation. 10 October. Accessed September 18, 2023. https://www.abc.net.au/news/2021-10-10/van-life-australia-live-cheaply-best-views/100520260.

cenex. 2021. “Refrigerated Transport Insights: A ZERO White Paper.” White Paper, Leicestershire.

Deutsche Gesellschaft für Internationale Zusammenarbeit (GIZ) GmbH . 2022. *Net-zero emission solutions for transport refrigeration in a sustainable cold chain .* Berlin: Deutsche Gesellschaft für Internationale Zusammenarbeit (GIZ) GmbH .

Dynge, Anders Steen-Nilsen, and Asbjørn Orheim Stoveland. 2013. *Optical Modellingfor Photovoltaic Panels.* Kristiansand: University of Agder.

Eke, Rustu, and Ali Senturk. 2012. “Performance comparison of a double-axis sun tracking versus fixed PV system.” *Solar Energy* 2665-2672.

ForgeSolar. n.d. *ForgeSolar Help.* ForgeSolar. Accessed October 2, 2023. https://www.forgesolar.com/help/.

Garde, Raquel, Fernando Jiménez, Tomás Larriba, Gabriel García, Mónica Aguado, and Manuel Martínez. 2012. “Development of a Fuel Cell-Based System for Refrigerated Transport.” *Energy Procedia* 29: 201-207.

Gordon, J M, Jan F Kreider, and Paul Reeves. 1991. “TRACKING AND STATIONARY FLAT PLATE SOLAR COLLECTORS: YEARLY COLLECTIBLE ENERGY CORRELATIONS FOR PHOTOVOLTAIC APPLICATIONS.” *Solar Energy* 47 (4): 245-252.

Honsberg, Christina, and Stuart Bowden. n.d. *PV Education.* Accessed September 10, 2023. https://www.pveducation.org/pvcdrom/properties-of-sunlight/solar-time#footnote1_9mgbfa2.

Ifaei, Pouya, Hasti Khiabani, Md Jalil Piran, and ChangKyoo Yoo. 2020. “Techno-econo-environmental feasibility of retrofitting urban transportation system with optimal solar panels for climate change mitigation - A case study.” *Journal of Cleaner Production* 251.

Janakeeraman, Suryanarayana Vasantha. 2013. *Angle of Incidence And Power Degradation Analysis of Photovoltaic Modules.* Tempe: Arizona State University.

King, D L, W E Boyson, and J A Kratochvill. 2004. *Photovoltaic Array Performance Model .* Albuquerque: Sandia National Laboratories .

King, David L, William E Boyson, and Jay A Kratochvil. 2002. *ANALYSIS OF FACTORS INFLUENCING THE ANNUAL ENERGY PRODUCTION OF PHOTOVOLTAIC SYSTEMS .* Albuquerque: Sandia National Laboratories.

Lightyear. n.d. *Light Year Two, Electric Driving Made Easy.* Lightyear. Accessed September 16, 2023. https://lightyear.one/lightyear-2.

Logan, Paula E., and Brian W. Raichle. n.d. "PERFORMANCE COMPARISON OF FIXED, SINGLE, AND DUAL AXIS TRACKING SYSTEMS FOR SMALL PHOTOVOLTAIC SYSTEMS WITH MEASURED DIRECT BEAM FRACTION." *Appalachian State University.*

Martin, N., and J. M. Ruiz. 2005. "Annual Angular Reflection Losses in PV Modules." *PROGRESS IN PHOTOVOLTAICS: RESEARCH AND APPLICATIONS* 75–84.

Masters, Gilbert M. 2013. *Renewable and Efficient Electric Power Systems.* Hoboken: John Wiley & Sons, Inc.

Meneghetti, Antonella, Fabio Dal Magro, and Alessandro Romagnoli. 2021. "Renewable energy penetration in food delivery: Coupling photovoltaics with transport refrigerated units." *Energy* 232.

Michael, Peter R., Danvers E. Johnston, and Wilfrido Moreno. 2020. "A conversion guide: solar irradiance and lux illuminance." *Journal of Measurements in Engineering,* 153–166.

Ota, Yasuyuki, Taizo Masuda, Kenji Araki, and Masafumi Yamaguchi. 2019. "A mobile multipyranometer array for the assessment of solar irradiance incident on a photovoltaic-powered vehicle." *Solar Energy* 84-90.

Pisanti, Cecilia. 2015. "Design and Energetic Evaluation of a Mobile Photovoltaic Roof for Cars." *Energy Procedia* 182-192.

Redekar, Abhijeet, Dipankar Deb, and Stepan Ozana. 2022. "Functionality Analysis of Electric Actuators in Renewable Energy Systems—A Review." *Sensors* 4273.

Schwarz, Winfried, Barbara Gschrey, André Leisewitz, Anke Herold, Sabine Gores, Irene Papst, Jürgen Usinger, et al. 2011. "Preparatory study for a review of Regulation (EC) No 842/2006 on certain fluorinated greenhouse gases."

She, Xiaohui, Lin Cong, Binjian Nie, Guanghui Leng, Hao Peng, Yi Chen, Xiaosong Zhang, Tao Wen, Hongxing Yang, and Yimo Luo. 2018. "Energy-efficient and -economic technologies for air conditioning with vapor compression refrigeration: A comprehensive review." *ScienceDirect* 232: 157-186.

Smolenaars, Kevin. 2021. *Presenting our newest solar-vehicle: Stella Vita!* Solar Team Eindhoven. 10 September. Accessed September 16, 2023. https://solarteameindhoven.nl/article?presenting-our-newest-solar-vehicle-stella-vita.

Solar Sena. 2021. *Solar Declination Angle & How to Calculate it.* Solar Sena. 26 April. Accessed October 10, 2023. https://solarsena.com/solar-declination-angle-calculator/.

Solargis. 2021. “Solar resource maps of World.” *Solargis.* Accessed September 2023, 19. https://solargis.com.

United States Environmental Protection Agency. 2022. “Diesel Emissions Reduction Act (DERA) Transport Refrigeration Unit (TRU) Factsheet.” November. Accessed September 19, 2023. https://nepis.epa.gov/Exe/ZyPDF.cgi/P1017V8N.PDF?Dockey=P1017V8N.PDF.

Vidyanandan, K. V. 2017. “An Overview of Factors Affecting the Performance of Solar PV Systems.” *Energy Scan (A house journal of Corporate Planning, NTPC Ltd.)* 2-8.

World Solar Challenge. n.d. *Bridgestone World Solar Challenge.* World Solar Challenge. Accessed September 17, 2023. https://worldsolarchallenge.org/.

Wu, Chien-Hsing, Hui-Chiao Wang, and Horng-Yi Chang. n.d. “Dual-axis solar tracker with satellite compass and inclinometer for automatic positioning and tracking.” *Energy for Sustainable Development* 308-318.

Yang , Zhuoqian , James E Tate, Eleonora Morganti , and Simon P Shepherd . 2021. “Real-world CO2 and NOX emissions from refrigerated vans.” *The Science of the Total Environment* 763.

Yellowhair, Julius, and Clifford K Ho. 2015. *ASSESSMENT OF PHOTOVOLTAIC SURFACE TEXTURING ON TRANSMITTANCE EFFECTS AND GLINT/GLARE IMPACTS.* Albuquerque: Sandia National Laboratories.

APPENDIX A

```
/* Script that tracks the sun with two steppers and LDRs. */

#include <Arduino.h>
#include <Stepper.h>
#include <OneWire.h>
#include <DallasTemperature.h>

/******************** PIN ALLOCATIONS ********************/
// Define stepper1 control pins
const int stepper1_ControlPin1 = 32;
const int stepper1_ControlPin2 = 33;

// Define stepper2 control pins
const int stepper2_ControlPin1 = 26;
const int stepper2_ControlPin2 = 27;

// LDR pins
const int LDR1 = 15;
const int LDR2 = 14;
const int LDR3 = 4;
const int LDR4 = 13;

// Data wire for DS18B20 temperature sensors is plugged into GPIO 16
#define ONE_WIRE_BUS 16

/******************** VARIABLE INITIALISATIONS ********************/
// Define number of steps per revolution, set to 2048 for 2 wire
control half stepping
const int stepsPerRev = 2048;

// Track step count of stepper1
int stepCount1 = 0;

// Direction of stepper1 rotation, used as input for steps to move in
.step() function
int stepDirection1 = 1;

// Max steps allowed for stepper1
int stepper1_maxSteps = 512;

// Track step count of stepper2
int stepCount2 = 0;

// Direction of stepper2 rotation, used as input for steps to move in
.step() function
```

```
int stepDirection2 = 1;



// Max steps allowed for stepper2
int stepper2_maxSteps = 0;

// LDR values
int LDR1_value = 0;
int LDR2_value = 0;
int LDR3_value = 0;
int LDR4_value = 0;

// Average LDR values
int LDR1_avg = 0;
int LDR2_avg = 0;
int LDR3_avg = 0;
int LDR4_avg = 0;

// Threshold brightness delta required before steppers will rotate
int LDR_threshold = 150;

// Used for averaging the values coming from LDRs to manage noise
int measurementCount = 10;

// Difference of LDR values on elevation axis
int LDR1_2_difference = 0;
int LDR3_4_difference = 0;

// Difference of LDR values on azimuth axis
int LDR1_3_difference = 0;
int LDR2_4_difference = 0;

// Difference of LDR values diagonals
int LDR1_4_difference = 0;
int LDR2_3_difference = 0;

// Setup a oneWire instance to communicate with temperature sensors
OneWire oneWire(ONE_WIRE_BUS);

// Pass oneWire reference to Dallas Temperature.
DallasTemperature sensors(&oneWire);

// Store temperature values of different panels
float flatTemp = 0.0;
float polarTemp = 0.0;
float twoAxisTemp = 0.0;

// Sensor addresses
```

```
DeviceAddress flatAddress = { 0x28, 0x07, 0x87, 0x4B, 0x21, 0x22, 0x09,
0x86 };
DeviceAddress polarAddress = { 0x28, 0xFC, 0xA1, 0x8F, 0x25, 0x22,
0x06, 0x80 };
DeviceAddress twoAxisAddress = { 0x28, 0x10, 0x50, 0x3C, 0x21, 0x22,
0x09, 0x79 };

// Number of temperature devices found
int numberOfDevices;

// Storing the address that are found
DeviceAddress tempDeviceAddress;

void printAddress(DeviceAddress deviceAddress);

/******************** STEPPER INSTANTIATIONS ********************/
// Instantiating stepper1 as a 2 wire controlled stepper
Stepper stepper1 = Stepper(stepsPerRev, stepper1_ControlPin1,
stepper1_ControlPin2);

// Instantiating stepper2 as a 2 wire controlled stepper
Stepper stepper2 = Stepper(stepsPerRev, stepper2_ControlPin1,
stepper2_ControlPin2);

/******************** FUNCTION PROTOTYPES ********************/
// Move and track steps of steppers
void moveAndTrackSteps(Stepper &stepper, int &stepCount, int
&stepDirection);

// Printing address of temperature sensors
void printAddress(DeviceAddress deviceAddress);

void setup()
{
  // Using serial monitor for debugging
  Serial.begin(115200);

  // Setting stepper speed in revolutions per minute
  stepper1.setSpeed(5);

  // Setting stepper speed in revolutions per minute
  stepper2.setSpeed(5);

  // Start up the temperature sensor library
  sensors.begin();
}

void loop()
{
```

```
  // Send the command to get temperatures
  sensors.requestTemperatures();

  // Store the current temperatures for each panel
  flatTemp = sensors.getTempC(flatAddress);
  polarTemp = sensors.getTempC(polarAddress);
  twoAxisTemp = sensors.getTempC(twoAxisAddress);

  Serial.print("Flat Temp: ");
  Serial.println(flatTemp);
  Serial.print("Polar Temp: ");
  Serial.println(polarTemp);
  Serial.print("2-Axis Temp: ");
  Serial.println(twoAxisTemp);

  for(int i = 0; i < measurementCount; i++)
  {
    // Read the LDRs
    LDR1_value += analogRead(LDR1);
    LDR2_value += analogRead(LDR2);
    LDR3_value += analogRead(LDR3);
    LDR4_value += analogRead(LDR4);

    delay(10);
  }

  LDR1_avg = LDR1_value/measurementCount;
  LDR2_avg = LDR2_value/measurementCount;
  LDR3_avg = LDR3_value/measurementCount;
  LDR4_avg = LDR4_value/measurementCount;

  // Calculating difference in average readings of LDRs on elevation
axis
  LDR1_2_difference = LDR1_avg - LDR2_avg;
  LDR3_4_difference = LDR3_avg - LDR4_avg;

  // Calculating difference in average readings of LDRs on azimuth axis
  LDR1_3_difference = LDR1_avg - LDR3_avg;
  LDR2_4_difference = LDR2_avg - LDR4_avg;

  // Calculating difference in average readings of LDRs on the
diagonals
  LDR1_4_difference = LDR1_avg - LDR4_avg;
  LDR2_3_difference = LDR2_avg - LDR3_avg;

/***** ELEVATION AXIS *****/

  // Check if the difference in average LDR readings in the elevation
angle (for both pairs) is above the threshold
```

```
  if(abs(LDR1_2_difference) > LDR_threshold && abs(LDR3_4_difference) > LDR_threshold)
  {
    // Check which direction is brighter and set the direction accordingly for stepper1
    if(LDR1_2_difference < 0 || LDR3_4_difference < 0)
    {
      stepDirection1 = -1;
    }
    else if(LDR1_2_difference > 0 || LDR3_4_difference > 0)
    {
      stepDirection1 = 1;
    }

    // Check if stepper1 is at its minimum (0 degrees) and is trying to move further in that direction
    if(stepCount1 == 0 && stepDirection1 == -1)
    {
      Serial.println("Stepper1 at min...");
    }
    // Check if stepper1 has reached its maximum angle (90 degrees or straight vertical) and is trying to move further in that direction
    else if(stepCount1 == stepper1_maxSteps && stepDirection1 == 1)
    {
      Serial.println("Stepper1 at max...");
    }
    else
    {
      // Move stepper1 in whichever direction specified by stepDirection1 and update stepCount1
      moveAndTrackSteps(stepper1, stepCount1, stepDirection1);
    }
  }

/***** AZIMUTH AXIS *****/

  // Check if the difference in average LDR readings in the azimuth angle (for both pairs) is above the threshold
  if(abs(LDR1_3_difference) > LDR_threshold && abs(LDR2_4_difference) > LDR_threshold)
  {
    // Check which direction is brighter and set the direction accordingly for stepper2
    if(LDR1_3_difference < 0 || LDR2_4_difference < 0)
    {
      stepDirection2 = 1;
    }
    else if(LDR1_3_difference > 0 || LDR2_4_difference > 0)
    {
```

```
      stepDirection2 = -1;
    }

    // Check if stepper2 is at its minimum (0 degrees) and is trying to
move further in that direction
    if(stepCount2 == -1024 && stepDirection2 == -1)
    {
      Serial.println("Stepper2 at min...");
    }
    // Check if stepper2 has reached its maximum angle (180 degrees)
and is trying to move further in that direction
    else if(stepCount2 == stepper2_maxSteps && stepDirection2 == 1)
    {
      Serial.println("Stepper2 at max...");
    }
    else
    {
      // Move stepper2 in whichever direction specified by
stepDirection2 and update stepCount2
      moveAndTrackSteps(stepper2, stepCount2, stepDirection2);
    }
  }

/***** FIRST DIAGONAL *****/

  // Check if the difference in average LDR readings in the first
diagonal is above the threshold and greater than the other diagonal
  if(abs(LDR1_4_difference) > LDR_threshold && abs(LDR1_4_difference) >
abs(LDR2_3_difference))
  {
    // Check which direction is brighter and set the direction
accordingly for both steppers
    if(LDR1_4_difference > 0)
    {
      stepDirection1 = 1;
      stepDirection2 = -1;
    }
    else
    {
      stepDirection1 = -1;
      stepDirection2 = 1;
    }

    // Check if stepper1 is at its minimum (0 degrees) and is trying to
move further in that direction
    if(stepCount1 == 0 && stepDirection1 == -1)
    {
      Serial.println("Stepper1 at min...");
    }
```

```
    // Check if stepper1 has reached its maximum angle (90 degrees or
straight vertical) and is trying to move further in that direction
    else if(stepCount1 == stepper1_maxSteps && stepDirection1 == 1)
    {
      Serial.println("Stepper1 at max...");
    }
    else
    {
      // Move stepper1 in whichever direction specified by
stepDirection1 and update stepCount1
      moveAndTrackSteps(stepper1, stepCount1, stepDirection1);
    }

    // Check if stepper2 is at its minimum (0 degrees) and is trying to
move further in that direction
    if(stepCount2 == -1024 && stepDirection2 == -1)
    {
      Serial.println("Stepper2 at min...");
    }
    // Check if stepper2 has reached its maximum angle (180 degrees)
and is trying to move further in that direction
    else if(stepCount2 == stepper2_maxSteps && stepDirection2 == 1)
    {
      Serial.println("Stepper2 at max...");
    }
    else
    {
      // Move stepper2 in whichever direction specified by
stepDirection2 and update stepCount2
      moveAndTrackSteps(stepper2, stepCount2, stepDirection2);
    }
  }

/***** SECOND DIAGONAL *****/

  // Check if the difference in average LDR readings in the second
diagonal is above the threshold and greater than the other diagonal
  if(abs(LDR2_3_difference) > LDR_threshold && abs(LDR2_3_difference) >
abs(LDR1_4_difference))
  {
    // Check which direction is brighter and set the direction
accordingly for both steppers
    if(LDR2_3_difference > 0)
    {
      stepDirection1 = -1;
      stepDirection2 = -1;
    }
    else
    {
```

```
      stepDirection1 = 1;
      stepDirection2 = 1;
    }

    // Check if stepper1 is at its minimum (0 degrees) and is trying to
move further in that direction
    if(stepCount1 == 0 && stepDirection1 == -1)
    {
      Serial.println("Stepper1 at min...");
    }
    // Check if stepper1 has reached its maximum angle (90 degrees or
straight vertical) and is trying to move further in that direction
    else if(stepCount1 == stepper1_maxSteps && stepDirection1 == 1)
    {
      Serial.println("Stepper1 at max...");
    }
    else
    {
      // Move stepper1 in whichever direction specified by
stepDirection1 and update stepCount1
      moveAndTrackSteps(stepper1, stepCount1, stepDirection1);
    }
  }

  // Reset the LDR values stored in memory to prepare to read again
  LDR1_value = 0;
  LDR2_value = 0;
  LDR3_value = 0;
  LDR4_value = 0;

  Serial.print("Stepper 1 count = ");
  Serial.println(stepCount1);
  Serial.print("Stepper 2 count = ");
  Serial.println(stepCount2);
}

/******************** FUNCTION DEFINITIONS ********************/
// Function to move and keep track of steps of steppers
void moveAndTrackSteps(Stepper &stepper, int &stepCount, int
&stepDirection)
{
  // Step 1 step in the relevant direction and update the step counter
  stepper.step(stepDirection);
  stepCount += stepDirection;
}

// Function to print a device address
void printAddress(DeviceAddress deviceAddress) {
  for (uint8_t i = 0; i < 8; i++){
```

```
    if (deviceAddress[i] < 16) Serial.print("0");
      Serial.print(deviceAddress[i], HEX);
  }
}
```